2010-12-17

Scanning Laser Registration and Structural Energy Density Based Active Structural Acoustic Control

Daniel Alan Manwill
Brigham Young University - Provo

Scanning Laser Registration and Structural Energy Density Based Active Structural Acoustic Control

Daniel A. Manwill

A thesis submitted to the faculty of
Brigham Young University
in partial fulfillment of the requirements for the degree of

Master of Science

Jonathan D. Blotter, Chair
Scott D. Sommerfeldt
Kent L. Gee

Department of Mechanical Engineering

Brigham Young University

April 2011

ABSTRACT

Scanning Laser Registration and Structural Energy Density

Based Active Structural Acoustic Control

Daniel Manwill

Department of Mechanical Engineering

Master of Science

To simplify the measurement of energy-based structural metrics, a general registration process for the scanning laser doppler vibrometer (SLDV) has been developed. Existing registration techniques, also known as pose estimation or position registration, suffer from mathematical complexity, instrument specificity, and the need for correct optimization initialization.

These difficulties have been addressed through development of a general linear laser model and hybrid registration algorithm. These are applicable to any SLDV and allow the registration problem to be solved using straightforward mathematics. Additionally, the hybrid registration algorithm eliminates the need for correct optimization initialization by separating the optimization process from solution selection. The effectiveness of this approach is demonstrated through simulated application and by validation measurements performed on a specially prepared pipe.

To increase understanding of the relationships between structural energy metrics and the acoustic response, the use of structural energy density (SED) in active structural acoustic control (ASAC) has also been studied. A genetic algorithm and other simulations were used to determine achievable reduction in acoustic radiation, characterize control system design, and compare SED-based control with the simpler velocity-based control.

Using optimized sensor and actuator placements at optimally excited modal frequencies, attenuation of net acoustic intensity was proportional to attenuation of SED. At modal and non-modal frequencies, optimal SED-based ASAC system design is guided by establishing general symmetry between the structural disturbing force and the SED sensor and control actuator. Using fixed sensor and actuator placement, SED-based control has been found to provide superior performance to single point velocity control and very comparable performance to two-point velocity control. Its greatest strength is that it rarely causes unwanted amplifications of large amplitude when properly designed.

Genetic algorithm simulations of SED-based ASAC indicated that optimal control effectiveness is obtained when sensors and actuators function in more than one role. For example, an actuator can be placed to simultaneously reduce structural vibration amplitude and reshape the response such that it radiates less efficiently. These principles can be applied to the design of any type of ASAC system.

Keywords: Daniel Manwill, scanning laser doppler vibrometer, registration, pose estimation, active structural acoustic control, structural vibration, acoustics, genetic algorithm

ACKNOWLEDGMENTS

I would like to thank my committee for their support in this endeavor and for the instruction and insights they provided throughout the research process. I would like to thank the department of Mechanical Engineering, and the National Science Foundation (Grant # 0826554) for the monetary support that made this work possible.

I would like to thank my wife Kathryn for her constant love and support, and for her many sacrifices in my behalf. I would like to thank my daughters Sarah, Rachel, and Eliza for all their smiles and hugs. I would like to thank my parents for encouraging my curiosity.

Finally, I would like to thank my Heavenly Father for giving us a universe governed by laws, and for providing us with the tools that allow us to discover and learn about them. I felt blessed and often inspired as I learned through this research about one tiny aspect of His great and magnificent creation.

TABLE OF CONTENTS

LIST OF TABLES

LIST OF FIGURES

NOMENCLATURE

A	Area of plate element
a	Plate x-dimension (chapter 3)
a, b	Subscripts indicating range (chapter 2)
b	Plate y-dimension (chapter 3)
C	Confidence
$\{C\}$	Direction of laser beam expressed in structural coordinates
D	Bending stiffness
d	Standoff distance
Δd	Change in standoff distance
D_{ij}	Actual distance between points i and j
D'_{ij}	Estimated distance between points i and j
dl	Mirror separation distance
D_{near}, D_{far}	Bounding standoff distances around structure
E	Elastic modulus (chapter 3)
$\{E\}$	Error vector (chapter 2)
E_R	Error in rotation matrix estimate
E_T	Error in translation vector estimate
E_2	Secondary error descriptor
F	Forcing complex amplitude (chapter 3)
F	Frequency of least-found distinct solution (chapter 2)

h	Parametric scaling (chapter 2)
h	Plate thickness (chapter 3)
i	Index of plate element (chapter 3)
$\bar{I}$	Acoustic intensity
$\{I\}$	General laser model intercept
i, j, k	Subscripts indicating point number (chapter 2)
I_x, I_y	General laser model intercept subcomponents
$[J]$	Jacobian matrix
j	$\sqrt{-1}$ (chapter 3)
L	Distance between moving origin and measured point
M	Difficulty multiplier
m, n	Modal indices
N	Number of registration points used, candidate solution pool size
new	Subscript indicating state of estimate
p	Complex pressure amplitude
$\{P_L\}$	Point location in laser coordinates
$\{\Delta P_L\}$	Change in laser coordinate
$\{P_S\}$	Point location in structural coordinates
$\{\Delta P_S\}$	Change in structural coordinate
previous	Subscript indicating state of estimate
$\{q\}$	Quaternion
Q_{mn}	Response scaling factor

q_1, q_2, q_3, q_4	Quaternion subcomponents
R	Distance (chapter 3)
r	Uniform random number between 0 and 1
$[R]$	Rotation matrix (chapter 2)
R_{12}	Rotation between first and second positions
R_{15}	Rotation between first and fifth positions
$\{S\}$	General laser model slope
$\{S'\}$	Estimated slope
t	Time
$\{T\}$	Translation vector
$\{T'\}$	Estimated translation vector
u, v, w	Unnormalized estimated slope components
unnormalized	Subscript indicating state of quaternion
v'	Moving origin location
V_n	Plate element complex velocity
W	Transverse displacement
w	Transverse displacement complex amplitude
x, y	Coordinate system bases
x_f	Forcing x-location
$\{x_L, y_L, z_L\}$	Principal axes of laser coordinate system
x_m	Measurement x-location
$\Delta x, \Delta y, \Delta z$	Change in x, y, and z (chapter 3)

$\Delta x_L . \Delta y_L , \Delta z_L$	Change in laser coordinates
y_f	Forcing y-location
y_m	Measurement y-location
θ_a , θ_b	Mirror angles
θ_{pitch}	Pitch mirror angle
ρ	Area density of plate
ρ_o	Density of air
υ	Poisson's ratio
ω	Driving frequency
ω_{mn}	Undamped natural frequency

1 INTRODUCTION

This chapter presents an introduction to the topics contemplated in this thesis. Background information and motivation for the work performed are presented, principal contributions are outlined, and the remaining thesis chapters are introduced.

1.1 General Area and Purpose of Research

This thesis presents the results of an effort to seek out better tools and more efficient metrics and methods to enable advances in the field of energy-based acoustics and vibration. Such advances facilitate better analysis and design by increasing understanding of physical phenomena and providing more universal means of describing and measuring them.

Efforts were directed first to the simplification of experimental measurement of energy-based structural vibration descriptors by development of a straightforward registration process for the scanning laser doppler vibrometer. Additional work was performed to characterize the relationship between control of one energy-based structural vibration descriptor, the structural energy density, and attenuation of acoustic radiation.

1.2 Scanning Laser Doppler Vibrometer Registration

Scanning laser doppler vibrometer (SLDV) registration addresses one of the challenges encountered in the study of structural energy metrics, namely the difficulty of experimental

measurements. Consider the measurement of structural intensity or power flow in a plate. Under certain restrictions on sensor proximity to energy sources and structural boundaries, it is possible to measure the structural intensity using only 4 accelerometers. However, if the desired measurement location does not meet the restrictions, then a full measurement should be made, requiring 13 or more accelerometers. This is an extensive and impractical undertaking, especially if many locations on the structure must be measured. In addition, the mass and damping added by sensors and cables can substantially alter the structural intensity pattern even if it does not alter the gross features of the structural response.

The process of vibration measurement is greatly improved by using an SLDV in place of discrete sensors such as accelerometers. The SLDV is a non-contact instrument which can quickly obtain complex velocity measurements at a large number of points on a structure without mass loading problems and without the tedium of moving large numbers of sensors. Post processing can be applied to the velocity data to obtain energy measurements. This post-processing requires as inputs the location of each point measured by the SLDV and the corresponding components of structural velocity measured. This information is obtained through the use of registration, which is also known as position registration or pose estimation.

A registration algorithm is an organized interaction among various elements, namely multiple coordinate systems, a model of the optical behavior of the SLDV, and an optimization routine. The end goal of a registration algorithm is to determine the coordinate transformation between the coordinate system of the SLDV and the coordinate system of the structure being measured. When the coordinate transformation is known, the spatial relationship of the SLDV and the structure is concretely defined and can be used to determine the intersecting location of the laser beam with the structure for each measured point as well as the components of velocity

detected. A technique such as spline fitting or Fourier analysis is then applied to the collection of velocity data points to create a sufficiently continuous mathematical description of the velocity field. This mathematical description of the velocity field can then be analyzed in terms of structural energy metrics by taking appropriate spatial and temporal derivatives and applying material properties.

Various registration techniques exist, being suited to different types of scanning lasers, and having various strengths and weaknesses. Several general difficulties exist in scanning laser registration and will now be described.

First, a conflict exists between registration accuracy and vibration measurement accuracy. To promote the accuracy of the registration solution, the structure would ideally be as close to the SLDV as possible in order to use the full angle range of the scanning mirrors. To promote accurate measurement of vibration, however, the structure should not be too close to the SLDV or the laser beam may have poor focus and strike the structure at high angles of incidence, reducing the signal-to-noise ratio. Balancing these two objectives often results in a smaller portion of the scanning mirror angle range being used than is optimal, and results in increased sensitivity to geometric error as the registration problem is solved.

The second general difficulty in registration is that the residual space in the optimization portion of most registration algorithms contains multiple minima. For a conceptual explanation of why this is so, consider Fig. 1-1, which shows a hypothetical measurement in two dimensions of two points A and B using a generic SLDV. The red lines represent the laser beams that intersect points A and B. The lightweight dotted lines are for geometric reference.

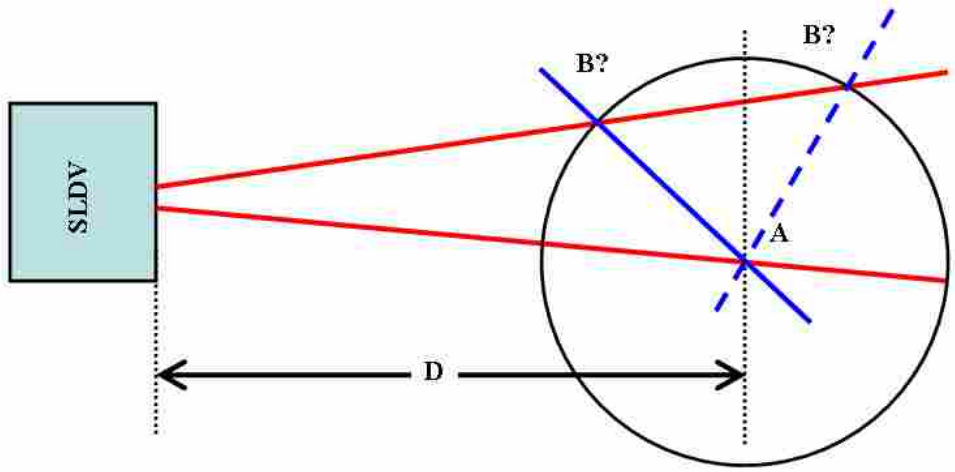

Figure 1-1: Two Solution Possibilities in Registration

In this example, point A is known to lie on the lower red line at a distance D from the SLDV. Point B is known to lie on the upper red line, but its distance from the SLDV is unknown. The distance from point A to point B is known, requiring it to be located somewhere on the black circle. This circle intersects the upper red line at two locations. The result is that the line connecting the true physical locations of A and B might be the solid blue line, but with equal likelihood, could be the dashed blue line. The spatial relationship between the SLDV and the measured points is not clearly defined by the conditions given.

In the example shown, it would not be difficult to compare the physical measurement setup with the two possible locations of B and select one as the correct location. However, in real-life measurement, geometry is three-dimensional and thus more difficult to visualize. Additionally, if the set of points measured has a poor aspect ratio or only subtends small angles, the different possible positions may be quite similar. As an example, in registration measurements performed on a pipe as described in Chapter 2, four possible positions of the structure were found. The variation in distance from the SLDV to the measured points among

these solutions was less than 5% of the mean distance to the points. Rather than being easily distinguished as in Figure 1-1, the four possibilities were effectively on top of each other.

In order to arrive at the correct solution, registration algorithms must either be designed to give only one solution, or be equipped to deal properly with multiple solution possibilities. The most straightforward method of achieving this is to use a laser rangefinder and directly measure the distance to each measured point, thus avoiding iterative optimization altogether. While this approach is very robust, it requires more equipment and time. Additionally, using extra equipment introduces additional calibrations and alignments which introduce their own inaccuracy into spatial data.

A second approach to obtaining the correct solution is to use the right starting point in optimization so that the correct solution is found first. However, this requires a companion method for generating the right starting guess, adding to complexity and difficulty. It also lacks a redundant check on the final answer should the "right" starting guess be wrong.

A third approach involves optimizing some quantity for which multiple minima exist, but can be easily distinguished as right or wrong. This type of algorithm provides some security to the user, but involves more difficult optimization processes. Although the right starting guess is not required in this case, a good starting guess is still required in order to avoid non-convergence problems in the awkward optimization space.

Regardless of the approach used in solving the registration problem, a third difficulty exists. Most if not all registration algorithms were developed with a specific SLDV in mind. Each SLDV will have its own model to describe its optical behavior. Depending on the optical model available for a specific instrument, it may be difficult or impossible to adapt to a registration algorithm developed for a different model of SLDV.

The objective of this research was to develop a registration method which was not difficult to use with different instruments, which used only simple math and optimization techniques, and which could deal with multiple minima more easily than existing techniques. The utility of this research lies in facilitating the measurement of structural energy metrics. Additional research was performed to study the application of a structural energy metric, namely structural energy density, in active structural acoustic control. This second focus will now be introduced.

1.3 Active Structural Acoustic Control and Structural Energy Density

Active structural acoustic control based on structural energy density (SED) is a specialization of active structural acoustic control (ASAC) which in turn is a specialization of active noise control (ANC). To give proper context to SED-based ASAC, the topics of ANC and ASAC are discussed first. Motivation for pursuing SED-based ASAC is then presented.

1.3.1 Active Noise Control

Active noise control is a broad field comprised of many methods and techniques generally used to reduce the negative effects of unwanted sound. ANC is an important supplement to passive noise control, especially at low frequencies. Passive methods are based on the selection, shaping, and placement of materials such that they absorb, block, or redirect the undesired sound. In general, the size and mass of these materials must increase as the controlled frequencies decrease. While small amounts of lightweight material are sufficient for controlling sound at high frequencies, large amounts of heavy material such as steel and concrete are required at low frequencies. In applications such as reducing the perception of engine noise

within an aircraft cabin, the use of such heavy materials is impossible and active methods must be used to maintain a suitable acoustic environment.

From a conceptual standpoint, the simplest ANC technique is that of creating the "opposite" sound wave to cancel out an undesired noise. This form of active noise control generally achieves noise reduction only in a small area around an error sensor. Another form of ANC involves reducing the ability of a noise source to transfer energy to its environment by altering its impedance. This form of ANC can achieve global attenuation for relatively compact noise sources of known location. A third form can be applied when the source of unwanted noise is a vibrating structure. This type of control is termed active structural acoustic control and is a key focus of this research.

1.3.2 ASAC

ASAC is a specialization of ANC that seeks to control sound by carefully managing the structural vibrations that cause the unwanted sound. It holds the promise of a more compact control system because sensors and actuators can be mounted on or within a structure rather than consisting of speakers and microphones spread throughout a volume. Additionally, it eliminates sound at its source before it has the opportunity to disperse into a larger volume where more sensors and actuators would be required to detect and control it.

ASAC can be more difficult to implement than other forms of ANC because, as frequently noted, control of the acoustic response is not perfectly correlated with control of the structural response. Much work has been performed to develop different varieties of ASAC using various sensors, actuators, and theories. A sampling of concepts is now presented.

Wang, Burdisso, and Fuller [1] studied the optimal placement of piezoelectric actuators for ASAC with acoustic error sensing. They concluded that actuators should be placed away

from nodal lines such that they can control multiple structural modes, especially those that contribute most efficiently to radiated sound.

Tan and Hird [2] studied the reduction of sound power radiated from a vibrating panel associated with reduction in panel vibration amplitude due to the action of an electromagnetic actuator. Their results showed that the greatest reduction in sound power was achieved when the actuator was placed at the center of the panel.

Cazzolato and Hansen [3] studied ASAC methods involving controlling the radiation modes of a structure. They showed that the output of a large number of structural vibration sensors could be decomposed into a smaller number of signals representative of radiation mode amplitudes. For large or modally dense structures, they recommended using a smaller number of film-type sensors each shaped to correlate with specific modes.

Ro and Baz [4] studied the use of patches of active constrained layer damping (ACLD) material in reducing the radiation of a vibrating structure into a cavity. Their results indicate that the ACLD, which inherently also possesses a passive component, can outperform passive constrained layer damping as well as active control by piezoelectric patches.

Sors and Elliott [5] ranked various types of sensors and actuators for use in ASAC. Their work indicated that volume velocity sensing and constant force actuation were most effective. As constant force actuation does not physically exist, they recommended the use of multiple piezoceramic actuator patches arranged so as to give a minimum phase system. They also indicate that using collocated piezo sensor-actuator pairs eliminates spillover, but often results in very poor performance because the piezo elements sense strain but not velocity.

Tanaka and Kobayashi [6] developed an active noise and vibration control system using acoustic error sensing and both acoustic and structural actuators. They were able to perform

acoustic potential energy control in an enclosure without spillover by use of cluster filtering. This was accomplished by grouping structural and acoustic modes according to their manner of interaction with each other. Each group was then sensed and controlled independently

Liu, Lee, and Lu [7] analyzed active and passive structural acoustic control for a box-type enclosure typical of a vehicle cabin. Their recommendations for sensor placement were based on the structural intensity in the panels forming the box. Using principles of conservation of energy, they indicate that virtual sinks in the structural intensity field are paths of energy coupling into the acoustic field. They recommend placing control actuators at these locations to disrupt the energy flow.

Although many variations of ASAC exist and utilize many types of sensors and actuators adapted to different applications, one fairly common theme is the inadequacy of trying to perform control based on a single point measurement. More effective methods attempt to create a larger area description of the structural response. Analysis is then performed to generate metrics that are based on whole-structure coupling to the adjoining acoustic space. As those metrics are controlled, the sound radiation and not just the amplitude of the structural response will be reduced. These types of metrics are based on concepts such as radiation modes, cluster filtering, and selective modal coupling. The assessment of these metrics requires multiple discrete sensors or a distributed sensor such as shaped PVDF film.

1.3.3 Structural-Energy-Density-Based ASAC

One concept that has not previously been tested for use in an ASAC system is the control of structural energy density. SED is a measure of the local total energy concentration in a vibrating structure. It is composed of a velocity-based term related to the kinetic energy density, and strain-based terms relating to the potential energy density. SED is a point-valued quantity,

and applying it to ASAC is in conflict with the cautions Sors and Elliott [5] give against using point sensors. However, SED possesses certain attributes which indicate it may actually perform successfully and provide an alternative to using large-area sensing.

First, as an energy-based quantity, SED may provide an approximation of the global response even though it is a point-valued measurement. A simple example of this type of effect is often applied in kinematics. The dynamic state of a large mechanism can be described by knowing the state of a single member when equivalence of kinetic energy is used to combine all components into a single effective element.

Second, SED incorporates aspects of spatial filtering. The use of spatial filtering in effective ASAC was emphasized in a review paper by Berry [8], who noted that such spatial filtering can be accomplished either by post-processing the outputs of a large number of discrete sensors or by using specially shaped sensors such as PVDF film. Measurement of SED requires either a small array of point sensors or a combination of point sensors and film-type sensors. In either case, some degree of spatial filtering would be included even though the sensor itself is comparatively compact.

Third, the control of acoustic energy density, the acoustic analogue of SED, has proven very successful in active noise control. Parkins *et al*. [9] applied the acoustic energy density to ANC in enclosures. They found that because it incorporates both potential and kinetic energies, the acoustic energy density provides a better approximation of the global response than pressure alone. In general, this resulted in increased attenuation and decreased sensitivity to sensor placement. SED is the same type of measurement, but in a structural domain. Application of SED in ASAC might also improve performance and generality of sensor placement.

Fourth, measurement of SED simultaneously captures both strain and velocity effects, both of which have been used for ASAC purposes.

1.4 Contributions

This thesis contributes to the areas of structural vibration and energy characterization measurement by scanning laser doppler vibrometry. Advantages over existing techniques were realized in part by development of a general linear laser model which possesses the following desirable attributes.

- Applicable to any SLDV
- Removes optical nonlinearities from the registration process
- Has an algebraic nature which simplifies registration mathematics
- Easy to invert

Additional benefits were gained through the incorporation of the new laser model into a hybrid registration algorithm which has the following attributes.

- Applicable to any SLDV
- Eliminates the need for laser rangefinders
- Eliminates the need for correct optimization initialization
- Mathematically straightforward
- Very stable

The thesis also contributes to the area of ASAC by presenting an analysis on the use of structural energy density in ASAC, a previously untested concept. The following topics are addressed and will be useful to those wishing to apply the technique or study it further.

- Controllability

- Proper sensor and actuator placement
- Ability to attenuate radiation
- Resistance to causing unwanted amplifications
- Comparison to velocity-based control

The analysis of SED-based ASAC also provided insights which are applicable to the design of any form of ASAC.

1.5 Thesis Outline

The remainder of this thesis is divided into three chapters. Chapters 2 and 3 represent manuscripts that will be submitted for journal publication.

Chapter 2 presents a general linear laser model and hybrid registration method developed in response to the second and third general difficulties associated with registration, which were described in Section 1.2 of this thesis. The first general difficulty described in Section 1.2 is not addressed by the general linear laser model or hybrid algorithm, but was mentioned for the benefit of those who apply the methods presented in this thesis without prior experience in the art.

The construction of Chapter 2 is as follows. The conceptual elements or building blocks of the registration process are explained. Current laser models and the general linear laser model are presented. Existing registration techniques are presented and their strengths and weaknesses are discussed. The hybrid registration algorithm is introduced. The mathematical process by which it solves the registration problem is presented in detail sufficient to facilitate implementation and demonstrate the utilization of the general linear laser model. A simulated test case is presented as validation for the proposed methods. An experimental test case is

presented which provides additional validation by comparison of multiple registration solutions. The chapter concludes with a brief explanation of how the registration solution is applied to the measured vibration data.

Chapter 3 presents work performed to characterize and guide the use of SED in ASAC. The construction of this chapter is as follows. ANC, ASAC, and the concept of using energy-based metrics are introduced. SED is defined and relevant previous applications are noted. The physical and mathematical models used in the simulation are presented. The controllability and mass-loading sensitivity of SED are established. The critical features of a genetic algorithm used to study sensor and actuator placement in SED-based ASAC are presented. Attenuation results and sensor and actuator placement guidelines arising from the genetic algorithm simulations are presented for modal and non-modal frequencies. Additional simulation is used to compare control effectiveness based on different design guidelines, and to compare SED-based control to velocity-based control. Results are interpreted in light of the guidance they provide to any type of ASAC design.

Chapter 4 is a concluding chapter which summarizes the main findings of the previous chapters, provides recommendations for future work, and briefly discusses several concepts which relate to future work but which did not fit within the framework of the journal manuscripts.

2 A HYBRID METHOD FOR SCANNING LASER REGISTRATION USING A GENERAL LINEAR LASER MODEL

This chapter presents a journal paper prepared for submission to Mechanical Systems and Signal Processing. Formatting of the paper has been modified to conform to thesis requirements.

2.1 Authors and Affiliations

D. Manwill[a] and J. Blotter[a]

[a]Department of Mechanical Engineering,
Brigham Young University,
435 Crabtree Building
Provo, Utah 84602

2.2 Abstract

Registration, also known as pose estimation and position registration, is an essential part of the accurate quantitative analysis of velocity data obtained with a scanning laser doppler vibrometer (SLDV). This paper presents a hybrid method of registration using a general linear laser model. The general linear laser model uses sets of slopes and intercepts rather than nonlinear functions of mirror angles to describe the spatial path of the laser beam. This simplifies registration mathematics and also allows the hybrid registration algorithm to be applied to any type of SLDV using any length unit system. The hybrid registration algorithm is comparable in accuracy to existing methods, but eliminates the need for laser rangefinders and the generation of high quality starting points in optimization. This is accomplished by using a

very stable optimization of a rotationally invariant property to generate a large number of potential solutions from random starting guesses, and then selecting the correct solution by means of a secondary error descriptor. Simulated and experimental validation is presented to support the effectiveness of this algorithm.

2.3 Subject Terms

scanning laser doppler vibrometer; pose estimation; position registration; vibration measurement.

2.4 Introduction

The scanning laser doppler vibrometer (SLDV) is a highly useful tool for analyzing the velocity response of vibrating structures. By acquiring and combining phased velocity amplitude measurements from many locations on a structure, it is able to produce a map of the overall structural velocity response. These maps can be used to determine mode frequencies and shapes and identify sources and transmission paths of vibration. Laser vibrometry also has specialized application outside the laboratory for purposes such as fault detection and quality control [10].

When the purpose of a measurement may be satisfied by a simple visual inspection of the velocity map, no further analysis is required. As is often the case, however, more quantitative analysis of data is desired for purposes such as comparison with finite element models or determination of structural energy metrics such as power flow [11]. Such analyses require precise information about the structural location of each point measured. Additionally, because the SLDV only detects the component of structural velocity parallel to the laser beam, capability to express the direction of the laser beam in terms of the structural coordinate system is needed so that amplitude and directional corrections can be made. While the structural location of

measured points can be determined manually by carefully measuring and recording the location where the laser beam hits the structure for each measured point, such processes are extremely tedious and add inconsistency to the data. Additionally, it is nearly impossible to easily and accurately determine the laser beam direction by manual means for all but the simplest measurements.

Fortunately, the use of a registration process allows for automated and consistent determination of both the structural location and the laser beam direction for each measured point. This is accomplished by proper characterization of the spatial relationship between the laser scanning head and the structure being scanned. Determination of this relationship is the main purpose of any registration algorithm.

The actual implementation of a registration algorithm is complicated by optical nonlinearities of the SLDV and multiple solution possibilities in optimization. This paper describes a general linear laser model and hybrid registration algorithm designed to deal with these difficulties in a manner that decreases the complexity of actual application in exchange for a small amount of computation time. Theory and background information are presented first, followed by the general linear laser model and hybrid registration algorithm. Simulated and experimental validations of the method are given, followed by a brief explanation of how measurement locations and laser beam directions may be obtained.

2.5 Theory

Registration is a topic which appears complex when taken as a whole. However, it is composed of relatively simple building blocks. These blocks consist of the SLDV and laser model, coordinate transformation and the coordinate systems of registration, and rotationally invariant properties. As the interaction of the blocks is what allows for solution of the

registration problem, a simultaneous comprehension of them is required in order to understand the registration process. For this reason, the blocks are each introduced first before presenting background and previous work in registration.

2.5.1 Block 1: The SLDV and the Laser Model

The SLDV is an optically-based vibration-detecting instrument which consists of a laser source, a pair of rotating mirrors, a decoder, and a camera. The mirrors are used to direct the laser beam to the desired measurement locations on the surface of a structure. The decoder interprets changes in interference between incident and reflected laser light to determine the magnitude and phase of the surface velocity at the laser spot location. The camera is used to facilitate selection of measurement locations and presentation of results.

As the rotating mirrors move the laser beam, its path through space is altered. A scanning laser model allows the path of the laser beam to be calculated given information about the rotation angles of the mirrors. In some cases, the laser model may require an additional step which computes mirror angles from the driving voltages of the potentiometers that cause the mirrors to rotate. When the range or distance to a measurement point from some reference point on the scanning head is known, the laser model will give the location of the measurement point $\{P_L\}$ in terms of the principal axes of the laser coordinate system, x_L, y_L, and z_L. Figure 2-1 shows a generic scanning head, a measurement point, the laser beam, and the laser coordinate system used in this paper. Note that the location of the origin and orientation of the axes can be altered for convenience as long as the same system is used throughout the entire registration process.

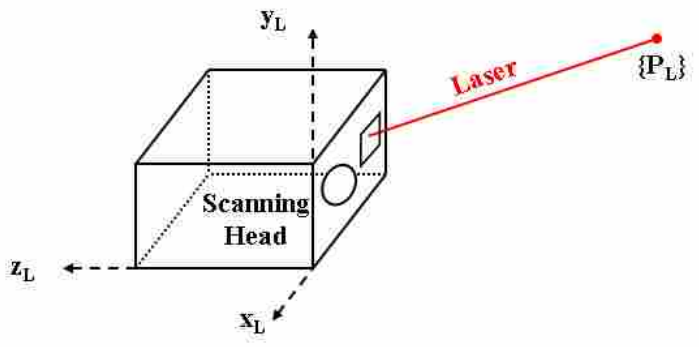

Figure 2-1: Laser Scanning Head and Coordinate System

The development of a laser model is complicated by the nonlinearities associated with using two mirrors to direct the laser beam. One mirror controls the vertical motion of the laser beam (pitch), while the other controls the horizontal motion (yaw). Due to the separation distance between the two mirrors, the apparent origin of the laser beam moves as the mirrors are rotated. Either the pitch or the yaw mirror will also have an additional nonlinearity in which although only one mirror is moved, both pitch and yaw of the laser beam are altered.

2.5.2 Block 2: Coordinate Transformations and Registration Coordinate Systems

A coordinate transformation provides a means of describing the physical location of a point with respect to different coordinate systems or reference frames. Mathematically, a coordinate transformation consists of a translation vector $\{T\}$ and rotation matrix $[R]$. $[R]$ and $\{T\}$ operate on the coordinates of a location in one frame to give the coordinates of the same location as seen in a second frame. The translation vector gives the location of the origin of the second frame with respect to the first frame. The rotation matrix is a square matrix, the number of columns being equal to the dimensionality of the coordinate system used. The n^{th} column gives the unit vector in the second coordinate system corresponding to the n^{th} axis of the first

coordinate system. The transpose of the rotation matrix is also its inverse and can be used to rotate coordinates from the second frame back into the first.

In addition to the coordinate system of the laser, registration involves the coordinate system associated with the structure being measured. As shown in Fig. 2-2, a measurement location which can be described by $\{P_L\}$ can also be described by $\{P_S\}$ when location is given in terms of the principal axes of the structural coordinate system. Although the structural coordinates can be described in polar or spherical coordinates for convenience, the hybrid registration algorithm requires that computation be performed using a Cartesian coordinate system.

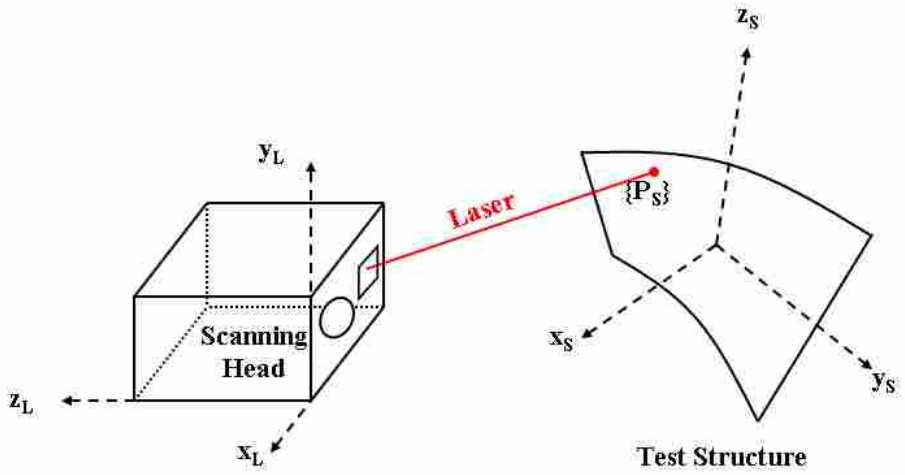

Figure 2-2: Scanning Head, Test Structure, and Their Coordinate Systems

As mentioned in Section 2.4, the key function of any registration algorithm is to define the spatial relationship between the SLDV and the test structure. This relationship is established by solving for the coordinate transformation given as

$$\{P_S\} = [R] * (\{P_L\} - \{T\}) \quad (2\text{-}1)$$

The inverse transform,

$$\{P_L\} = [R]^T * \{P_S\} + \{T\}, \tag{2-2}$$

is also needed. The process of determining the coordinate transformation will described in Section 2.9.4.

2.5.3 Block 3: Rotationally Invariant Properties

A rotationally invariant property is a property of a set of points that does not change when the expressed locations of the points are subjected to a coordinate transformation. Examples include but are not limited to the distance between any two points, the dot product of any two rays formed by connecting points, and the geometric properties of a triangle formed by any three points. Rotationally invariant properties are an important part of many registration algorithms.

2.6 Laser Model Overview

As explained in Section 2.5.1, registration requires a model of the scanning laser optical behavior to give the path of the laser beam through space for a given set of mirror angles. This model must capture the two-mirror nonlinearities described. The instrument manufacturer will sometimes provide a model for their instrument in equation form. One example of an equation-based model was used by Zeng *et al.* [12], and is given with a few changes in notation as

$$\{P_L\} = \begin{Bmatrix} L\sin(\theta_a) \\ (L\cos(\theta_a) - dl)\sin(\theta_b) \\ (L\cos(\theta_a) - dl)\cos(\theta_b) \end{Bmatrix}. \tag{2-3}$$

The notation used is as follows: L is the distance from the moving origin to the measurement point, dl is the separation distance between the mirrors, and θ_a and θ_b are the mirror angles associated with the same point.

A different type of model was used by Lindholm [13]. Rather than calculating laser spot location by a modified trigonometric relation as is done in Eq. 2-3, the physical location of the moving origin, v', was calculated as

$$v' = \begin{Bmatrix} -0.135 \\ 0.153 + 0.046\sin\left(\theta_{pitch}\right) \\ 0.067 - 0.046\cos\left(\theta_{pitch}\right) \end{Bmatrix} \tag{2-4}$$

based on the pitch angle, θ_{pitch} of the scanning mirrors. The law of cosines was then used in connection with other geometric features of the test setup to give definition to the laser spot location. Equation 2-4 has units of meters, and again, its notation has been slightly modified.

For Polytec® SLDV systems, the laser model equations are not provided, but the coordinates $\{P_L\}$ can be obtained by setting the results viewer to 3-D mode, inputting a range estimate, and exporting scan data. This capability is sufficient for registration with the general linear laser model.

In cases where a manufacturer-provided model is unavailable, it may be possible through careful manual alignment and measurement to fit equations or develop an empirical model. In practice, an empirical model may be as accurate as the equations supplied by the manufacturer, as it can account for the effects of manufacturing deviation and calibration drift.

All of the laser models described above are instrument specific and may be termed primary models. Two principal difficulties arise in the incorporation of these primary models into the registration process. First, should one possess multiple instruments, multiple sets of registration code would be required. Second, these models are often difficult to invert. Inversion

is the process of back-calculating mirror angles or equivalent information from measurement point locations. When using a typical primary model, this will often require iterative measures because of the coupling between pitch, yaw, and the moving origin.

The general linear laser model proposed here may be termed a secondary model. It does not eliminate the need for a primary model. The primary model is needed to derive the parameters of the secondary model, a process performed for each registered measurement. Once the secondary model parameters have been determined, registration calculations proceed without further need of the primary model. This allows registration code to be universal rather than instrument-specific. Additionally, it simplifies the mathematics of working with the inverted laser model. The general linear laser model and the method for deriving its parameters from the primary model are now presented.

2.7 The General Linear Laser Model

The general linear laser model is intended to serve as a computational replacement for the primary laser model of any SLDV. This model is based on the idea that because a laser beam is a straight line through space, the beam of any scanning laser can be represented by the equation of a line regardless of the underlying optics. The form of linear equation chosen is composed of a three-dimensional slope vector $\{S\}$, a three-dimensional intercept vector $\{I\}$, and the distance, d, of the laser spot on the structure from the plane defined by $z_L = 0$, measured perpendicular to that plane. These three parameters are the input into

$$\{P_L\} = d\{S\} + \{I\}, \tag{2-5}$$

by which the laser spot location, $\{P_L\}$, is calculated. The distance d will hereafter be termed standoff distance. Equation 2-5 is the general linear laser model.

Each registration point will have its own $\{S\}$ and $\{I\}$, which are calculated using the instrument-specific primary model as follows. Two arbitrary but distinct ranges, d_a and d_b are selected and the underlying primary laser model is used to calculate the corresponding laser spot positions $\{P_L\}_a$ and $\{P_L\}_b$ given the mirror angles associated with that registration point. The slope term $\{S\}$ for the registration point can then be calculated as

$$\{S\} = \begin{Bmatrix} \Delta x_L / \Delta z_L \\ \Delta y_L / \Delta z_L \\ 1 \end{Bmatrix}, \tag{2-6}$$

in which Δx, Δy, and Δz are given by

$$\begin{Bmatrix} \Delta x_L \\ \Delta y_L \\ \Delta z_L \end{Bmatrix} = \{P_L\}_a - \{P_L\}_b \quad . \tag{2-7}$$

The intercept is then calculated as

$$\{I\} = \begin{Bmatrix} I_x \\ I_y \\ 0 \end{Bmatrix} = \{P_L\}_a - d_a\{S\} \quad . \tag{2-8}$$

Figure 2-3 shows how the parameters in the general linear laser model, or the variables from which they are derived, relate to the geometry of the scanning head and laser beam. The variables Δx_L, Δy_L, and Δz_L can be thought of as defining the signed edge lengths of a box which is aligned with the scanning head coordinate system and which has the laser beam passing through diagonally opposite corners. The intercept terms I_x and I_y give the location where the laser beam breaks the plane defined by $z_L = 0$.

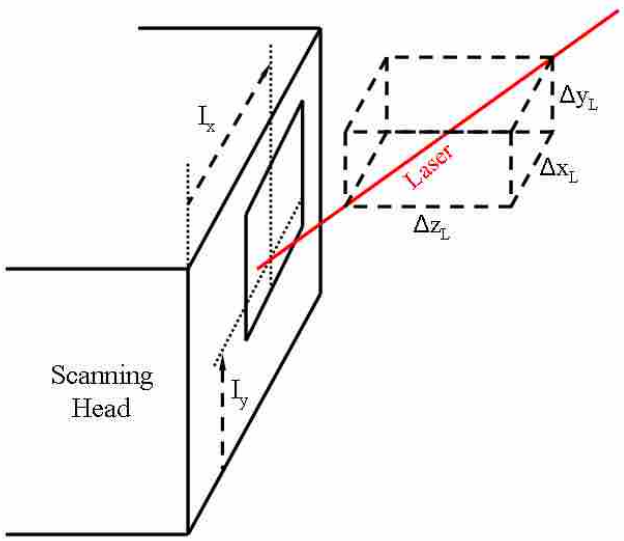

Figure 2-3. Scanning Head Geometry, Laser Beam, and General Linear Laser Model Parameters

The operations shown in Eqs. 2-6 through 2-8 are performed to calculate $\{S\}$ and $\{I\}$ for all registration points. Depending on the accuracy and precision of the underlying primary laser model, it may be necessary to keep d_a and d_b well-separated to reduce error when calculating the $\{S\}$ and $\{I\}$ parameters of the secondary model. As a check on calculations, the third component of $\{I\}$ should always be zero. Note that for a Polytec® SLDV, $\{P_L\}_a$ and $\{P_L\}_b$ are obtained by direct export from the software without the explicit inclusion of mirror angles in the process.

If the available primary laser model does not fit the calculations described, the general linear laser model can still be applied. The process of determining $\{S\}$ and $\{I\}$ is simply one of using two points along the laser beam to compute the slope-intercept form of a line in Cartesian 3-space. The slope term is then normalized such that the independent variable is the perpendicular distance from the plane defined by the front of the SLDV.

The general linear laser model differs from traditional optical-behavior-based models in the following ways. First, the direction of the laser beam is represented by slopes rather than

mirror angles. This allows pitch and yaw to be uncoupled mathematically because the terms of $\{S\}$ are not dependent on each other. Second, moving origin effects are captured with a constant intercept term rather than as a function of the mirror angles. This allows origin and directional parameters to be uncoupled mathematically. Third, the general linear laser model ignores nonlinear optical behavior. A change in mirror angles will have a non-linear effect on the laser beam path, but a change in slope or intercept will have a linear effect mathematically. The combined benefits of linearity and decoupling are especially advantageous when working with an inverted laser model. The inversion of a model refers to working backwards to determine what mirror orientation was needed to hit a certain point in space. In this regard, it is much simpler to back-calculate for slopes (or the intercept, if desired) than to back-calculate for mirror angles. Note that although primary models can be put in slope-intercept form, benefits of decoupling, universality, and algebraic inversion are not achieved.

2.8 Registration Algorithms

Registration algorithms are used to determine the spatial relationship between an SLDV and the structure being measured. This is accomplished by finding enough of the terms in Eq. 2-1 that the remainder can be solved for. This typically requires marking points of known coordinates on the structure (termed registration points) and recording the mirror angles required to direct the laser beam to those locations. This could also be accomplished through computer vision techniques [14]. The registration points become a collection of $\{P_S\}$'s, and although the corresponding $\{P_L\}$'s are not known *a priori*, the laser model can be applied to determine the spatial path on which they reside. A third piece of information must then either be measured or estimated in order to solve the transformation problem. Registration algorithms are primarily differentiated by what tertiary information they employ. Three main variations exist.

2.8.1 Existing Registration Algorithms

The first type of algorithm uses the range of each registration point from some point on the SLDV as the third input. Range information is obtained with a laser rangefinder attached to or incorporated in the laser scanning head. With range information known, the laser model can be used to obtain the laser coordinate $\{P_L\}$ of each registration point. Since the location of all registration points is thereby known in both laser and structural coordinate systems, the rotation matrix and translation vector can be solved for by using point correspondences and iterative techniques. The use of this registration technique was presented by Montgomery and West [15].

This method is very robust against gross errors in the coordinate transformation solution. However, it also requires extra equipment and may require extra time. The use of additional equipment introduces additional calibrations and thus increases potential for inaccuracy.

The second type of registration algorithm also employs the registration point ranges as a third input, but these are determined in an iterative manner by requiring equality of a suitable rotationally invariant property rather than being measured directly. One example of this type of algorithm is presented by Zeng *et al.* [12]. Although almost any rotationally invariant property could be employed, the distance between paired registration points is typically used.

The second type of algorithm is very stable. Unfortunately, the optimization space for a rotationally invariant property will contain at least two minima, and according to this author's findings, as many as four depending on how registration points are arranged. While a search can be made to find the minima with global minimum error in the property being minimized, it will actually be the wrong solution in a small percentage of cases for most rotationally invariant properties. The use of this type of algorithm then requires some additional method for obtaining the right starting estimate of ranges so that the algorithm does not arrive at the wrong solution.

The third type of algorithm does not employ ranges but rather involves direct iterative estimation of $[R]$ and $\{T\}$. This is accomplished by requiring equality of the scanning mirror angles as recorded for the registration points and as back-calculated from the transformation estimate and inverted laser model. A good example of this type of algorithm was given by Lindholm [13]. As with the second type of algorithm, multiple minima exist in the optimization space. Although the global minimum error solution is the correct solution in this case, good starting guesses are still required to avoid convergence problems due to the highly dynamic nature of the optimization space. This method also requires numerical derivatives when using a traditional laser model.

2.8.2 A Proposed Hybrid Registration Algorithm

This paper proposes a two-part hybrid method of registration that draws upon the strengths of the second and third types of registration algorithms. These modifications are designed to eliminate some of the weaknesses of existing methods, namely the need for laser rangefinders and correct or even good optimization initialization. The hybrid algorithm was designed to be used with a minimum of user input. The hybrid method will be developed in detail in Section 2.9.

2.8.3 A Comparative Summary of Registration Algorithms

Type 1

- Tertiary information: Ranges by direct measurement using rangefinder
- Strengths: Straightforward and robust
- Weaknesses: Additional equipment and potential for inaccuracy

Type 2

- Tertiary information: Ranges by iterative optimization of distance
- Strengths: Stable and straightforward
- Weaknesses: Requires correct initialization of optimization

Type 3

- Tertiary information: Transformation matrices by iterative matching of inverted laser model
- Strengths: Minimum error optimization solution is the correct solution.
- Weaknesses: More difficult to code and optimize. Poor performance when adapted to the general linear laser model.

Hybrid Method

- Tertiary information: Many iterative optimizations of distance followed by solution selection using the inverted general linear laser model.
- Strengths: Stable and straightforward. Does not require good optimization initialization or rangefinders.
- Weaknesses: Slightly higher computation times

2.9 The Hybrid Registration Algorithm

The hybrid registration algorithm is a multi-stage process for determining the coordinate transformation between laser and structural coordinate systems. It requires at least four registration points. Figure 2-4 is a flowchart describing the steps of the hybrid registration process. Stage 1, or preparation, is performed only once. Stage 2, or candidate solution creation, is repeated as many times as necessary to generate a complete solution pool. The general linear

laser model is not a step, process, or subroutine of the hybrid registration algorithm, but is a common mathematical foundation shared throughout all parts of the registration process.

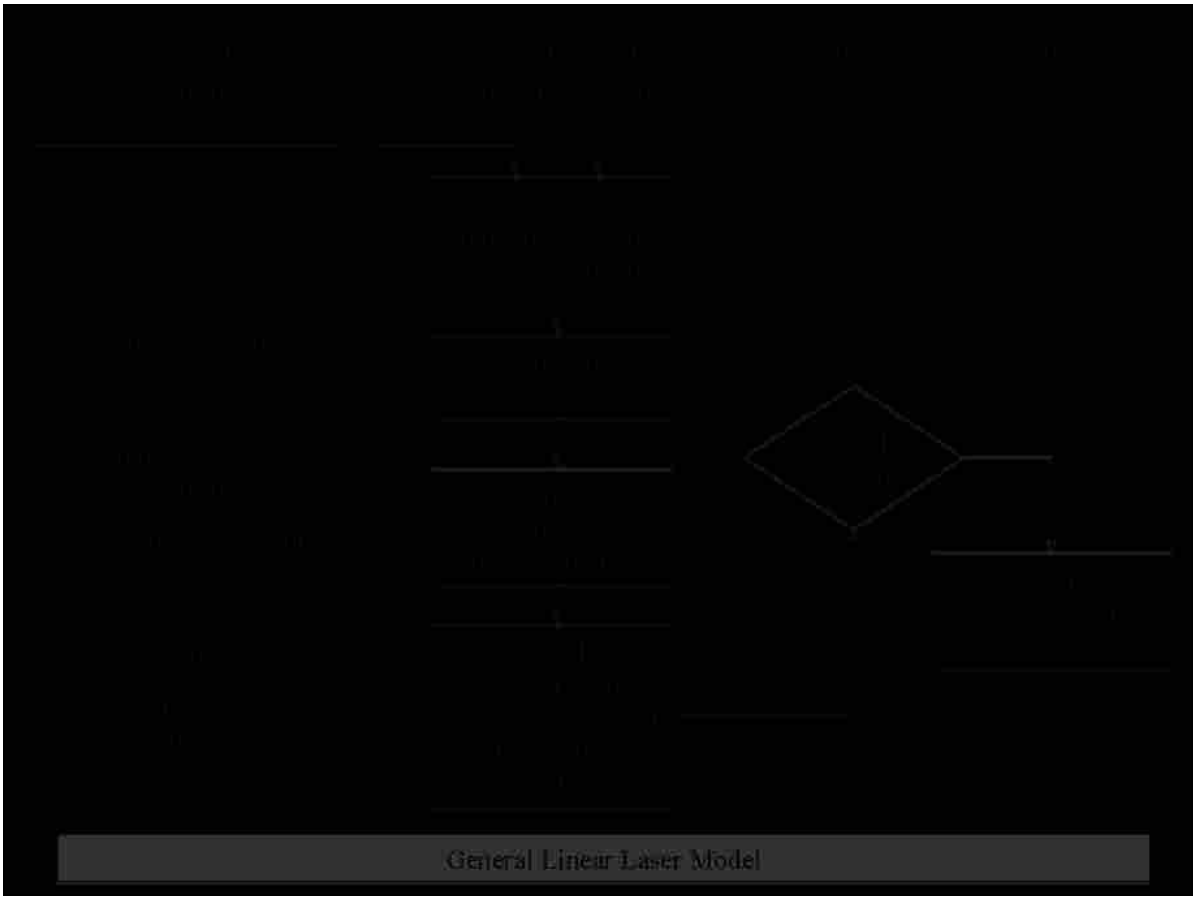

Figure 2-4. Hybrid Registration Process Flowchart

The mathematical presentation given in subsequent sections is more thorough than is typical when describing a registration algorithm. The author's purpose is to demonstrate the high level of integration possible between the general linear laser model and the hybrid registration algorithm. This integration is advantageous. It allows the solution to proceed without the use of cumbersome and sensitive numerical derivatives, an inconvenient necessity for some existing registration algorithms.

2.9.1 Stage 1: Preparation

The seven steps of the preparation stage of the registration process will now be described in detail. Steps 1-4 and 6 are common to almost all SLDV registration algorithms. Steps 1 and 2 are typically performed only once.

1. A convenient structural coordinate system is defined.
2. A set of N≥4 well-separated, non-collinear points are marked on the surface of the structure, and their locations with respect to the structural coordinate system are measured and recorded. These points are called registration points. For a discussion of the proper placement of registration points on a structure, see Martarelli *et al*. [16].
3. The laser scanning head is situated relative to the structure.
4. The laser beam is directed to each registration point, and corresponding mirror angles are recorded.
5. The distance between the z_L=0 plane and the closest registration point on the test structure is divided by two and recorded as D_{near}. The distance between the z_L=0 plane and the most remote registration point on the test structure is multiplied by 1.5 and recorded as D_{far}. According to the definitions used, these distances are negative. Only rough estimates are required.
6. Without moving the scanning head or structure, the desired vibration measurements are carried out. Mirror angles (or equivalent information) for each measured point are saved, along with the desired vibration descriptors.
7. The primary laser model is used to calculate $\{S\}$ and $\{I\}$ for each registration point according to Eqs. 2-6 through 2-8.

2.9.2 Stage 2, Step 1: Generation of Standoff Distance Starting Estimates

A standoff distance starting estimate for each registration point is created as follows. First, a random number r is drawn from a uniform distribution between 0 and 1. The associated starting distance estimate, d_i, for the registration point is then calculated using

$$d_i = -\left(D_{near} + r(D_{far} - D_{near})\right). \tag{2-9}$$

The subscript i indicates the i^{th} registration point. These distance estimates are just an initialization for optimization, and do not coincide with the actual or expected standoff distances.

2.9.3 Stage 2, Step 2: Standoff Distance Optimization

The standoff distance starting estimates for all registration points are optimized in an iterative manner until the geometric distances between points as viewed from the laser reference frame are as similar as possible to the actual distances calculated from the known structural locations of the registration points. The following process is used.

First, the laser-reference location for each registration point is estimated by applying

$$\{P_L\}_i = d_i\{S\}_i + \{I\}_i \tag{2-10}$$

to the range estimate and secondary laser model slopes and intercepts. The actual distance D_{ij} between the i^{th} and j^{th} registration points is then calculated as

$$D_{ij} = \sqrt{\left\langle \{P_S\}_i - \{P_S\}_j \right\rangle \bullet \left\langle \{P_S\}_i - \{P_S\}_j \right\rangle} \tag{2-11}$$

for all possible combinations of i and j. The estimated distance D'_{ij} between the i^{th} and j^{th} registration points is then also calculated as

$$D'_{ij} = \sqrt{\left\langle \{P_L\}_i - \{P_L\}_j \right\rangle \bullet \left\langle \{P_L\}_i - \{P_L\}_j \right\rangle} \tag{2-12}$$

for all possible combinations of i and j. Finally, the error E_{ij} for each distance estimate is calculated by applying

$$E_{ij} = D_{ij} - D'_{ij}. \tag{2-13}$$

The next step of the process is to calculate the partial derivatives of the error for each registration point pair with respect to the relevant standoff distance estimates. This is accomplished by substituting the general linear laser model expression for $\{P_L\}$ into Eq. 2-12, then substituting the result into Eq. 2-13 and taking partial derivatives with respect to the standoff distances. This results in

$$\frac{\partial E_{ij}}{\partial d_i} = \left(\frac{-1}{D'_{ij}}\right)\left(\left(\{P_L\}_i - \{P_L\}_j \bullet \{S\}_i\right)\right), \tag{2-14}$$

$$\frac{\partial E_{ij}}{\partial d_j} = \left(\frac{1}{D'_{ij}}\right)\left(\left(\{P_L\}_i - \{P_L\}_j \bullet \{S\}_j\right)\right), \tag{2-15}$$

and

$$\frac{\partial E_{ij}}{\partial d_k} = 0, k \neq i, j, \tag{2-16}$$

in which k is simply another index variable. These partial derivatives are assembled into a matrix [J] by matching each i-j point pair to a row, and matching the standoff distance of each registration point to a column as shown by

$$J = \begin{bmatrix} \frac{\partial E_{12}}{\partial d_1} & \frac{\partial E_{12}}{\partial d_2} & \cdots & \frac{\partial E_{12}}{\partial d_N} \\ \frac{\partial E_{13}}{\partial d_1} & \frac{\partial E_{13}}{\partial d_2} & \vdots & \vdots \\ \vdots & \vdots & \ddots & \vdots \\ \frac{\partial E_{N-1,N}}{\partial d_1} & \cdots & \cdots & \frac{\partial E_{N-1,N}}{\partial d_N} \end{bmatrix}. \tag{2-17}$$

An incremental change in the standoff distance estimate, $\{\Delta d\}$, is then calculated as

$$\{\Delta d\} = \left([J]^T [J]\right)^{-1} [J]^T \{E\}, \tag{2-18}$$

and subsequently used to improve the standoff distance estimate by

$$\{d\}_{new} = \{d\}_{previous} - \Delta d \,. \tag{2-19}$$

The calculation of Eqs. 2-10 through 2-19 is repeated until the norm of $\{\Delta d\}$ is very small. For example, the norm of $\{\Delta d\}$ at convergence may be a few nanometers even though the structure is a few meters from the SLDV and the standoff distances themselves are only accurate to a centimeter. This high level of convergence does not materially change the registration results, but it does make pool evaluation easier. Pool evaluation is discussed in Section 2.9.6.

2.9.4 Stage 2, Step 3: Determination of the Transformation

After the completion of step 2, a final estimate of $\{P_L\}$ for each registration point is obtained by Eq. 2-10. The registration transformation can then be calculated through an iterative process by making use of the equivalence between each $\{P_L\}_i$ and the corresponding $\{P_S\}_i$.

The process of determining the transformation begins with the calculation of the vectors connecting all pairs of registration points. The connecting vectors are given by

$$\{\Delta P_S\}_{ij} = \{P_S\}_j - \{P_S\}_i \tag{2-20}$$

in the structural coordinate system, and

$$\{\Delta P_L\}_{ij} = \{P_L\}_j - \{P_L\}_i \tag{2-21}$$

in terms of the laser coordinate system.

Using these connecting vectors, it is possible to determine the transformation in two stages. The rotation matrix is calculated first. Various formulations exist for defining a rotation

matrix, but a quaternion formulation is used in this work due to its mathematical stability, analytic nature, and lack of trigonometric ambiguity associated with some angle-based formulations. The quaternion, represented as $\{q\} = \{q_1, q_2, q_3, q_4\}$ is a unit vector composed of four constants. The quaternion is normalized to unit length by

$$\{q\} = \frac{\{q_{unnormalized}\}}{\|q_{unnormalized}\|}. \tag{2-22}$$

The corresponding rotation matrix is then given as

$$[R] = \begin{bmatrix} q_1^2 - q_2^2 - q_3^2 + q_4^2 & 2q_1q_2 + 2q_3q_4 & 2q_1q_3 - 2q_2q_4 \\ 2q_1q_2 - 2q_3q_4 & -q_1^2 + q_2^2 - q_3^2 + q_4^2 & 2q_2q_3 + 2q_1q_4 \\ 2q_1q_3 + 2q_2q_4 & 2q_2q_3 - 2q_1q_4 & -q_1^2 - q_2^2 + q_3^2 + q_4^2 \end{bmatrix}. \tag{2-23}$$

To solve for the quaternion, a random guess for $\{q\}$ is generated, normalized, and used to generate a rotation matrix. The error for each point pair, E_{ij}, due to error in the quaternion is calculated as

$$\{E_{ij}\} = [R]\{\Delta P_L\}_{ij} - \{\Delta P_S\}_{ij}, \tag{2-24}$$

and the partial derivative of the error is calculated by

$$\left\{\frac{\partial E_{ij}}{\partial q_k}\right\} = \left[\frac{\partial R}{\partial q_k}\right]\{\Delta P_L\}_{ij}. \tag{2-25}$$

The J matrix is then assembled as

$$J = \begin{bmatrix} \frac{\partial E_{12}}{\partial q_1} & \frac{\partial E_{12}}{\partial q_2} & \frac{\partial E_{12}}{\partial q_3} & \frac{\partial E_{12}}{\partial q_4} \\ \frac{\partial E_{13}}{\partial q_1} & \frac{\partial E_{13}}{\partial q_2} & \vdots & \vdots \\ \vdots & \vdots & \ddots & \vdots \\ \frac{\partial E_{N-1,N}}{\partial q_1} & \cdots & \cdots & \frac{\partial E_{N-1,N}}{\partial q_4} \end{bmatrix}. \tag{2-26}$$

An incremental change in the quaternion, $\{\Delta q\}$, is subsequently given by

$$\{\Delta q\} = \left([J]^T [J]\right)^{-1} [J]^T \{E\}, \tag{2-27}$$

and the quaternion estimate is the updated according to

$$\{q\}_{new,unnormalized} = \{q\}_{previous} - \{\Delta q\}. \tag{2-28}$$

The calculation of Eqs. 2-22 through 2-28 is then repeated until convergence is achieved, with the quaternion being re-normalized at the end of each iteration. The partial derivative of the [*R*] matrix in Eq. 2-25 is composed term-by-term by taking the derivative of the corresponding term in the [*R*] matrix. Note that *J* and *E* stand generically for Jacobian matrix and error vector respectively, and will be different in each stage of the algorithm.

When the quaternion optimization has converged, the translation vector is determined. First, an estimated translation,

$$\{T'\}_i = \{P_L\}_i - [R]^T \{P_S\}_i, \tag{2-29}$$

is calculated for each registration point. The final estimate of translation is then obtained by

$$\{T\} = \frac{1}{N} \sum_{i=1}^{N} \{T'\}_i, \tag{2-30}$$

which is simply an averaging operation.

2.9.5 Stage 2, Step 4: Calculation of the Secondary Error Metric

Application of the equations of steps 1-3 of the second stage of registration results in a candidate solution to the registration problem. As mentioned in reference to the second type of registration algorithm, the solution with the least residual error in optimization may not actually be the correct solution when a rotationally invariant property has been minimized. The outcome of the fourth step presented here is that each candidate solution is assigned an additional error descriptor which facilitates the selection of the correct solution. This descriptor is based on an

inversion of the general linear laser model and matching of predicted slopes with actual slopes. It is similar in nature to the angle-matching of Lindholm's algorithm [13], but does not involve a primary laser model and only checks the inverted laser model parameters rather than undertaking the arduous task of trying to optimize for them. The solution with the minimum in this secondary metric will be the correct solution.

The process by which the secondary error descriptor is calculated is as follows. First, Eq. 2-5 is substituted into Eq. 2-2. Then, the intercept term $\{I\}$ is moved to the right hand side, and $d_i\{S\}_i$ is replaced by $\{u,v,w\}_i$. This results in

$$\begin{Bmatrix} u \\ v \\ w \end{Bmatrix}_i = [R]^T * \{P_S\}_i + \{T\} - \{I\}_i \quad , \tag{2-31}$$

in which the subscript i again corresponds to the i^{th} registration point. The predicted slopes $\{S'\}_i$ are calculated by

$$\{S'\}_i = \begin{Bmatrix} u/w \\ v/w \\ w/w \end{Bmatrix} . \tag{2-32}$$

After the predicted slopes have been calculated for all registration points, the secondary error metric E_2 for the candidate solution can be determined by

$$E_2 = \sum_{i=1}^{N} (\{S\}_i - \{S'\}_i)^T (\{S\}_i - \{S'\}_i) . \tag{2-33}$$

This secondary error metric gives an indication of the scannability of the candidate solution by answering the question, "How much would the laser beam slopes need to change to hit the location of each registration point as predicted by the coordinate transformation?".

2.9.6 Selection of the Correct Solution

Steps 1 through 4 of stage 2 are repeated many times while generating a pool of candidate solutions. Before the correct solution can be selected, the pool must be cleaned and must be complete. If the pool is deemed complete after being cleaned, the correct solution can be selected as the one with the lowest value of E_2. If the pool is deemed incomplete, more candidate solutions are generated. The process of generating solutions, cleaning the pool, and judging completeness is repeated until the desired level of certainty is achieved that the correct solution has been found.

The pool is cleaned by removing candidate solutions that are inherently wrong. These solutions fall into two categories. The first is the unconverged solution, in which the standoff distance optimization of Eqs. 2-10 through 2-19 was terminated not by convergence, but by reaching the maximum allowable number of iterations. The second is the mirror solution, in which the predicted coordinate transformation places the measured object behind the scanning head rather than in front of it. Unconverged solutions are rare unless a large number of registration points have been used. When four or five points are used, the standoff distance optimization will typically converge to better than one part in a million (change in the norm of $\{\Delta d\}$) in fewer than 15 iterations.

Once the pool has been cleaned, a judgment of completeness is made. The pool is complete when it can be expected to contain solutions corresponding to all distinct minima which exist in the region of optimization space bounded by D_{near} and D_{far}. If the pool is incomplete, then the candidate solution with the lowest E_2 value may or may not be the correct solution and more solutions should be generated.

To aid in making this judgment, a plot of the E_2 values of all candidate solutions in the cleaned pool sorted in ascending order is particularly helpful. An example is given as Fig. 2-5, and would be interpreted as follows. The pool contains 20 clean candidate solutions. Among these are found three distinct values of E_2: 3×10^{-5}, 1.3×10^{-4}, and 2.2×10^{-4}, which are repeated 10, 4 and 6 times respectively. This indicates that, at present, three distinct minima have been found in the standoff distance optimization space. The middle minimum is the most difficult to "find", comprising only 20% of the solution pool. The first and third minimum account for 50% and 30% of the solution pool respectively.

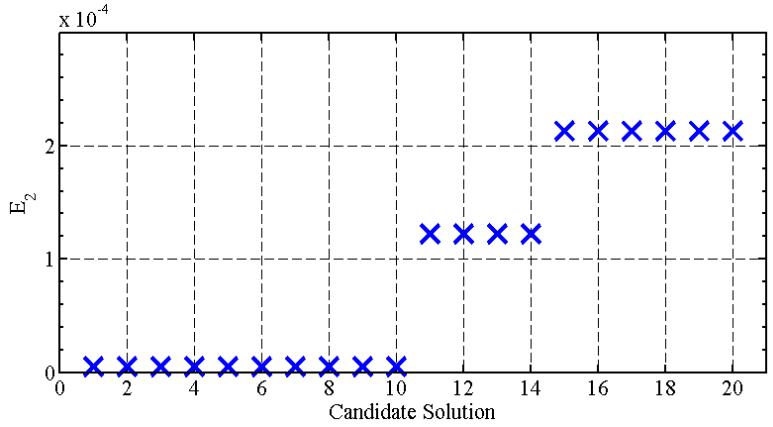

Figure 2-5: Sorted E_2 Values of a Small Candidate Solution Pool

Typically, the pool is grown to anywhere between 60 and 200 candidate solutions, with the sorted E_2 plot being used to evaluate the state of the pool after every batch of 20 solutions. The relative proportions of the distinct solutions in the pool will vary while the pool is small, but will stabilize as the pool becomes complete. When the relative proportions of the distinct solutions have stabilized, it is an indication that the random starting guesses have given uniform coverage to the standoff distance optimization space. A few more solutions may be generated

for added confidence and then the pool is deemed complete and the generation of candidate solutions is discontinued.

The process of deciding if the pool is complete could be compared to repeatedly rolling a die which has a small, but unknown number of sides in order to determine the smallest number on the die. The die is rolled many times until the roller is assured that all sides have been seen. The smallest number encountered is then deemed to be the smallest number on the die.

If preferred, a statistical approach can be taken to quantify the probability of pool completeness. Consider again the pool described by Fig. 2-5. Assuming a fourth minimum existed and was ten times more difficult to find than the middle solution, there would be a 98% chance of not finding it with any randomly generated starting guess. The probability of not finding it in 20 solutions is then 67%, indicating that more than 20 candidate solutions should probably be generated. If after the generation of 500 candidate solutions, a fourth distinct solution had not been found and the relative frequency of the three original solutions remained the same, the probability of having missed a fourth solution under the same assumptions would be 0.0041%.

This type of reasoning can be used to automate the algorithm by terminating pool growth when

$$\left(1-\frac{F}{M}\right)^{N} < (1-C), \tag{2-34}$$

and N is greater than some minimum pool size, rather than by visual inspection. In this formula, F is the frequency of the least-found distinct solution, M is the difficulty multiplier, N is the size of the pool, and C is the desired confidence that all distinct solutions have been found. Based on assumptions about the difficulty of finding additional distinct solutions, the pool can be grown as large as necessary to satisfy the user that the pool is complete. Regardless of which method is

used to determine pool completeness, the correct registration solution in a complete pool will be the one with the lowest value of E_2.

2.10 Comments on Hybrid Registration

This section provides high-level information on the hybrid algorithm.

2.10.1 Objectives and Mathematical Implementation

Hybrid registration may not be the most efficient, accurate, or mathematically elegant registration algorithm. It was not designed to meet those objectives. It was designed for universality, for simplicity to the end user, for implementation without using ambiguous trigonometry or any math more complex than matrix inversion, and especially for the elimination of rangefinders and carefully generated starting guesses.

The mathematical methods presented are not unique to the hybrid registration algorithm, nor is the hybrid algorithm restricted to implementation by the mathematics presented. Gauss-Newton iteration and the pseudo-inverse method were used for optimization, but other methods could have been employed. The use of a quaternion in describing rotation is by no means original, nor required. The mathematical implementation presented, however, is the recommended implementation because it is stable, straightforward, and relatively efficient, makes good use of the general linear laser model, does not require numerical derivatives or any tuning of optimization parameters, and allows the algorithm to run as a black box.

In its purest form the hybrid algorithm is simply the union of a very stable optimization process that cannot discern between correct and incorrect solutions, with a secondary criterion that does have discerning capability but is difficult to optimize directly. Any mathematical

implementation that fits this description could be considered a hybrid algorithm, but some of the benefits described in this section may be lost.

2.10.2 Achieving Efficiency

When using a small number of registration points, a very large candidate solution pool can still be generated quickly if excessive confidence is desired. As an example, a basic laptop computer running MATLAB code was able to produce candidate solutions for a four-registration-point problem at a rate of 2000 per minute. With large numbers of registration points, however, it will be more efficient to solve the problem by generating the candidate solution pool using four or five registration points and selecting an initial solution. Then, substitute Eq. 2-5 into Eq. 2-2 and solve for d. Use the resulting equation and $[R]$ and $\{T\}$ from the initial solution to calculate d for all registration points, and use those values as the starting standoff distance estimates to perform a final standoff distance optimization and transformation solution for all registration points.

Becoming familiar with the general nature of standoff distance optimization spaces and the growth of the candidate solution pool will allow one to use the hybrid algorithm most effectively. Developing an instinct for answers to questions like "How many distinct solutions are typically found for the geometries I work with?" will help the user apply the algorithm with confidence without generating an excessive number of candidate solutions. Familiarity may be gained most rapidly by randomly generating a large number of test cases and observing patterns in pool growth as they are solved.

The standoff distance estimates D_{near} and D_{far} can also influence algorithm efficiency. The exact values of these distance estimates are not critical; their purpose is simply to define a bounding box around the structure. Even estimates made by walking off the distance from the

SLDV to the structure will be sufficiently accurate. If the dimensions of a structure are small relative to the structure's distance from the SLDV, a box defined by applying step 5 of stage 1 described in Section 2.9.1 may be unnecessarily large and the starting guesses will be too spread out. This will result in a slight increase in iteration count and thus computation time. It may also promote the generation of mirror solutions. On the other hand, if the box is too small, it may restrict the starting guesses such that not all distinct candidate solutions will be found.

2.11 Simulated Application

To demonstrate the application of the hybrid registration algorithm, a simulated test case is presented. The test case is based on a coordinate transformation defined by

$$q = \frac{[10,2,3,1]}{\sqrt{114}}, \tag{2-35}$$

$$R = \begin{bmatrix} 0.7719 & 0.4035 & 0.4912 \\ 0.2982 & -0.9123 & 0.2807 \\ 0.5614 & -0.0702 & -0.8246 \end{bmatrix}, \tag{2-36}$$

$$T = \begin{Bmatrix} 0.2 \\ -0.3 \\ -8.0 \end{Bmatrix}, \tag{2-37}$$

and a set of five registration point locations which are given in Table 2-1. These were invented based on experience with what is typically encountered in laboratory measurements of modestly sized structures. The registration points form a rectangular pyramid shape. Gaussian random noise with a standard deviation of 0.02 was added to the registration point structural locations to represent the inaccuracy introduced by imperfect marking and targeting. Slopes and intercepts were not derived from any primary laser model, but as this is a mathematical exercise, were simply calculated so as to satisfy other geometric constraints. Note also that because of the

universality of the general linear laser model, it was not necessary to specify a length units system for the simulated geometry.

Table 2-1: Simulated Registration Point Locations and Laser Model Parameters

Point	*Assumed Structural Location*	*Actual Structural Location*	*Slopes*	*Intercepts*
1	0,0,0	0.033, -0.009, -0.022	-0.0206, 0.0281, 1.0	0.046, -0.053, 0
2	3,0,0	3.012, 0.024, -0.020	-0.3635, -0.1231, 1.0	0.159, 0.095, 0
3	0,2,0	0.006, 1.999, 0.013	-0.0964, 0.2654, 1.0	0.090, -0.146, 0
4	3,2,0	2.992, 1.987, -0.005	-0.4898, 0.1357, 1.0	0.176, -0.095, 0
5	1.5,1,0.5	1.533, 0.993, 0.519	-0.2475, 0.0737, 1.0	0.140, -0.079, 0

The hybrid registration algorithm was applied to this point set. The first four points were included in the initial transformation estimate, and the fifth was added for a final optimization. Figure 2-6 shows how the number of distinct solutions in the pool grew for the simulated test case as the pool size was increased from 1 to 2000 candidate solutions. The pool contained two distinct solutions at four total solutions, and no more were found in the remaining 1996 solutions generated. In practice, less than 200 candidate solutions would have been generated.

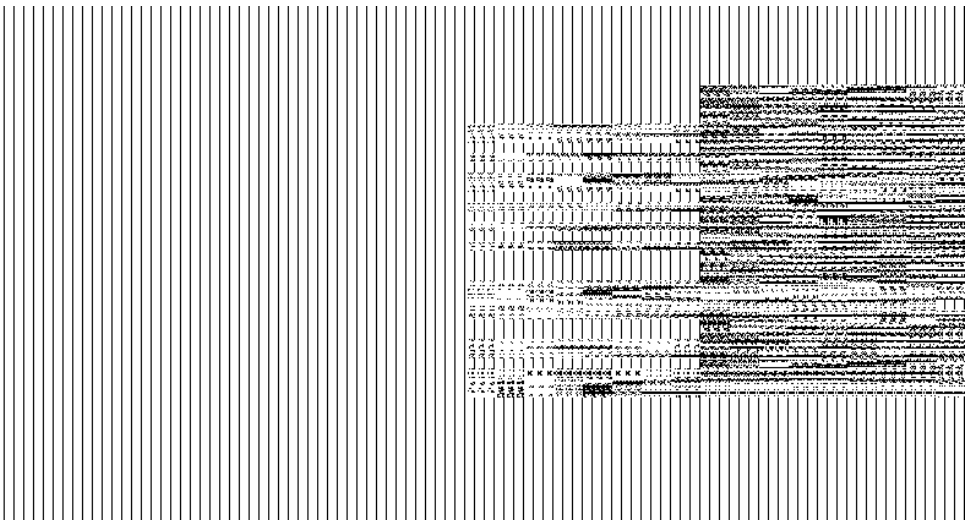

Figure 2-6: Number of Distinct Solutions vs. Pool Size, Simulated Case

The rotation matrix and translation vector resulting from the solution of the simulated registration problem are given as

$$R = \begin{bmatrix} 0.7725 & 0.4008 & 0.4925 \\ 0.2894 & -0.9126 & 0.2889 \\ 0.5653 & -0.0806 & -0.8210 \end{bmatrix} \tag{2-38}$$

and

$$T = \begin{Bmatrix} 0.225 \\ -0.287 \\ -8.0358 \end{Bmatrix} \tag{2-39}$$

respectively. The error in these results as compared to the actual transformation is given by

$$E_R = \begin{bmatrix} -0.0006 & -0.0027 & -0.0013 \\ 0.0089 & 0.0003 & -0.0081 \\ -0.0039 & 0.0104 & -0.0036 \end{bmatrix} \tag{2-40}$$

and

$$E_T = \begin{Bmatrix} -0.0250 \\ -0.0130 \\ 0.0358 \end{Bmatrix}. \tag{2-41}$$

The error is entirely due to the noise added to the simulated registration point locations.

2.12 Experimental Validation

To demonstrate the application of the hybrid registration algorithm using actual data, registration was performed using a PSV-400 SLDV and a 4 inch nominal size ABS plastic pipe. The average outer diameter of the pipe was measured at 114.8 mm. The midsection of the pipe was marked with a regular grid of registration points. Four rows of points with 150 mm spacing were used in the axial direction, and 8 columns of points with 37.5 degree average spacing were

used in the radial direction. A glitter-doped adhesive was used to mark the registration points so that it would be more readily apparent when the laser beam was aligned with each one. Although the use of a rectangular grid of registration points conflicts with the recommendation of Martarelli *et al*. [16] that registration points not be placed on vertical or horizontal lines, the number of registration points used was sufficient to obtain an accurate solution.

Figure 2-7 shows the pipe, portable optics bench, SLDV scanning head, and SLDV controller used for this experiment. Figure 2-8 shows a close-up of the base of the pipe and the alignment fixture assembled on the optics bench. The scale attached to the pipe is a centimeter ruler which was laser printed at 0.9393 magnification. The pipe was maintained in tangential contact with the two larger brackets to approximate a fixed center of rotation. The bracket on the left was aligned with the scale to control the rotation angle. Up to 16 of the 48 registration points on the pipe were accessible in the SLDV's field of view at any time.

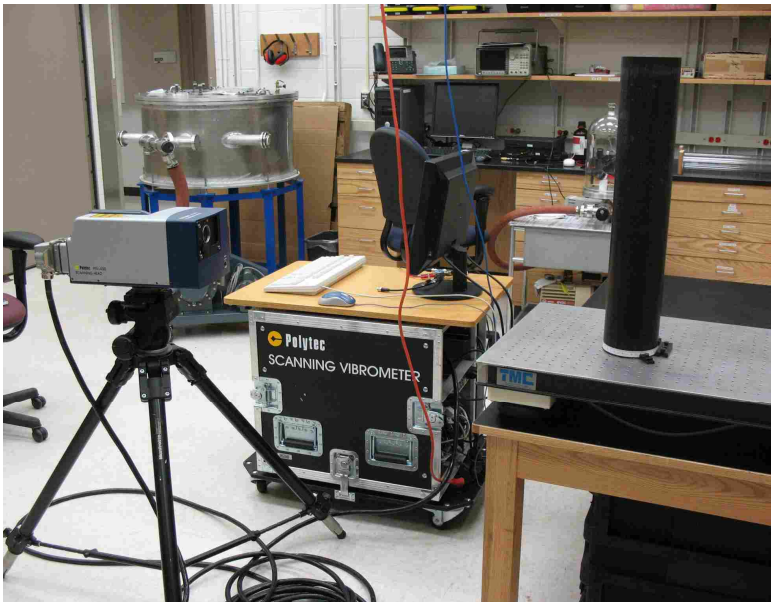

Figure 2-7: Registration Setup

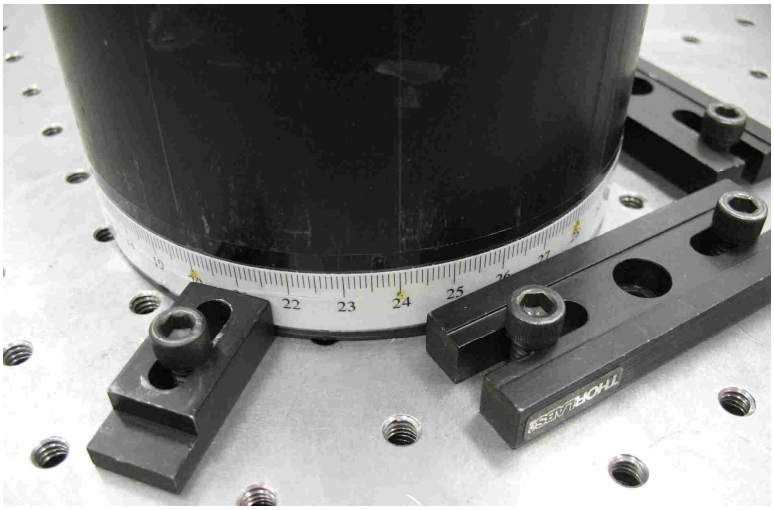

Figure 2-8: Pipe Fixtures and Scale

One of the difficulties in the experimental validation of a registration algorithm is that the actual registration transformation is unknown and hence unavailable for use in assessing the accuracy of results as it would be in simulation. Notwithstanding careful manual alignment of the test structure and scanning head, it is very difficult to obtain a manual coordinate transformation estimate for which the accuracy is comparable to the numeric accuracy of a registration algorithm. With these limitations in mind, two evidences for the validity of the hybrid registration method are presented.

First, as was done by Lindholm [13], the algorithm is shown to interact with physical data in like manner to simulated data. The assertion is then made that because the algorithm can be proven to work in simulation, it must also work in practice.

The second type of evidence is unique to this paper and is based on the idea of comparative registration. For any experimental registration solution, the actual coordinate transformation is unknown. If after an initial registration, however, the structure or SLDV is moved in some well-defined manner and a second registration procedure is performed, the

coordinate transformation that converts one registration solution to the other should match the physical movement of the experimental setup.

To perform the second type of validation, the laser scanning head was left stationary and registration was repeated several times, the pipe being rotated about its *z*-axis between measurements. The increment of rotation was approximately 37.5 degrees in each case. As the pipe was slightly out-of-round, the exact increments of rotation will vary slightly.

The first type of evidence is presented in Fig. 2-9, which shows the increase in the number of distinct solutions as the candidate pool was grown to excess proportions. Four distinct solutions were found with the first four random starting guesses, and no additional distinct solutions were found in the next 1996 solutions generated. This indicated that the algorithm interacted with experimental data in like manner to simulated data, and that all distinct solutions were found quickly.

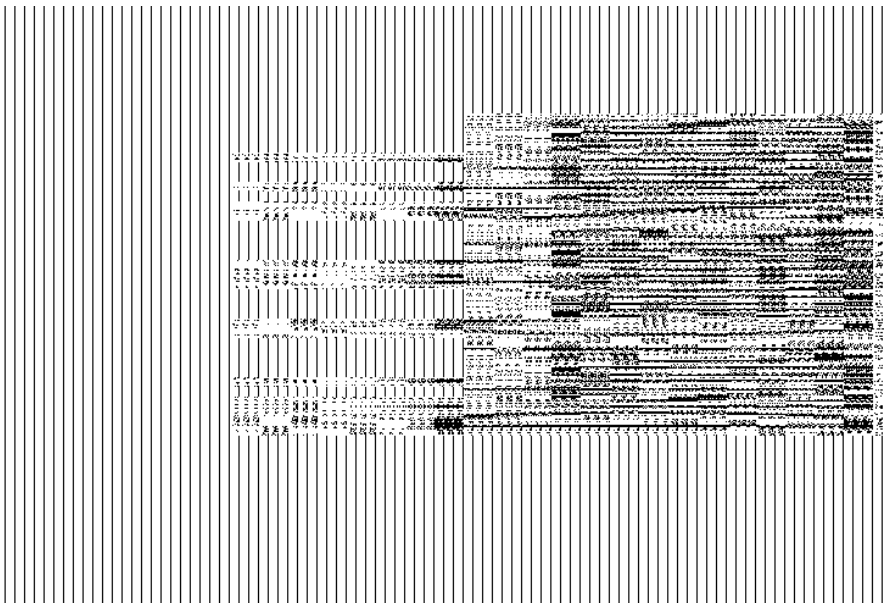

Figure 2-9: Number of Distinct Solutions vs. Pool Size, Experimental Case

The second type of evidence related to comparison of registration at multiple positions is now presented.

$$R_{12} = \begin{bmatrix} 0.7865 & -0.6176 & 0.0005 \\ 0.6175 & 0.7864 & -0.0141 \\ 0.0083 & 0.0114 & 0.9999 \end{bmatrix} \tag{2-42}$$

is the rotation matrix that maps between the rotation matrices of the first and second registration solutions, and

$$R_{15} = \begin{bmatrix} -0.8636 & -0.5035 & 0.0258 \\ 0.5038 & -0.8638 & 0.0067 \\ 0.0189 & 0.0188 & 0.9996 \end{bmatrix} \tag{2-43}$$

is the rotation matrix that maps between the rotation matrices of the first and fifth registration solutions. Both matrices have values very close to one in the lower right corner, indicating a nearly pure rotation about the z-axis, as expected. The angles of rotation for these matrices can be approximated by taking the inverse cosine of the upper left term in each matrix. For the first matrix, the resulting rotation angle is 38.1 degrees. This compares favorably to the expected rotation of 37.5 degrees. For the second rotation matrix the predicted rotation is 149.7 degrees, which is very close to the expected rotation of 150 degrees. Although the actual registration solutions are unknown, it can be inferred that they are correct because the relationships between the individual registration solutions would not match the physical movements of the pipe if they were in gross error.

2.13 Applying Registration Results

This section gives an overview of how to calculate measurement point locations and laser beam directions using the solution of the registration problem and the general linear laser model.

These processes are applied to the points at which velocity measurements were taken (stage 1, step 6, Section 2.9.1).

The laser beam direction for each measurement point as expressed in the laser coordinate system is simply the general linear laser model slope term $\{S\}$ for that point as calculated using Eqs. 2-6 through 2-8. However, it is more useful to express the beam direction in the structural coordinate system and convert it to a unit vector. This vector is denoted as $\{C\}$ and is calculated by

$$\{C\} = \frac{[R]\{S\}}{\left|[R]\{S\}\right|}. \tag{2-44}$$

Determining the structural coordinates of a measured point can be readily accomplished by using the general linear laser model to express the equation of the laser beam line in structural coordinates. The location of the measured point is then found by mathematical intersection of the laser beam line equation with an analytical description of the structure's geometry. The equation of the laser beam line expressed in slope-intercept form is

$$\{P_S\} = h\{C\} + [R](\{I\} - \{T\}), \tag{2-45}$$

in which h is simply a parametric scaling which serves the same purpose as d in Eq. 2-5 but is no longer the perpendicular distance from the z_L=0 plane. If the shape of the structure cannot be described with a single analytical function, it can be decomposed into elements or facets which can individually be approximated by analytical functions.

If the structure has two possible intersection locations with the laser beam line (i.e. a cylinder, sphere, ellipsoid, etc) the correct intersection can be found by a two-step process. In the first, the value of h (deemed h_1) corresponding to the location on the laser beam nearest the center of rotation of the structure is determined. A bisection-type search is then performed for

the intersection of the beam line and structural surface, with the search domain being bounded by h=0 and h=h_1. This excludes the far-side intersection from the search region.

2.14 Conclusions

A general linear laser model and hybrid registration algorithm have been presented which were developed to simplify the application of registration. The successful implementation of these techniques on simulated data was presented. Evidence was also given to support its functionality in the experimental domain through calculation of the rotation between the coordinate transformations of multiple registration solutions.

The principal strength of the hybrid registration algorithm is use of a two-stage process which eliminates the need for good or even correct starting guesses and laser rangefinders. The mathematical development presented also allows the algorithm to be used as a black box without the need for tuning numerical derivatives or convergence parameters. The use of the general linear laser model has the additional benefit of allowing all stages of the registration process and solution application to be seamlessly integrated regardless of the instrument used.

The principal weakness of the hybrid registration algorithm is that slightly higher computation times are required because of the large number of iterative solutions that must be computed. However, computation time should generally be less than 1 minute, making the method suitable for research applications. Guidelines were given to aid in efficient application of the hybrid algorithm and prevent excessive computation time.

Future development of the hybrid algorithm could include efforts to correlate the arrangement of the registration points on a structure with the number of expected distinct minima in the candidate solution pool.

3 ACTIVE STRUCTURAL ACOUSTIC CONTROL USING STRUCTURAL ENERGY DENSITY

This chapter presents a journal paper prepared for submission to Applied Acoustics. Formatting of the paper has been modified to conform to thesis requirements.

3.1 Authors and Affiliations

Daniel Manwill[a], Scott Sommerfeldt[b], Jonathan Blotter[a], and Kent Gee[b]

[a]Department of Mechanical Engineering,
Brigham Young University,
435 Crabtree Building
Provo, Utah 84602

[b]Department of Physics and Astronomy
Brigham Young University,
N283 ESC
Provo, UT 84602

3.2 Abstract

Multiple simulations have been used to determine the design and performance implications of the application of structural energy density (SED) to active structural acoustic control (ASAC). SED was found to have properties ideal for minimization by conventional control algorithms. A genetic algorithm used to study sensor and actuator placement indicated that both should be placed in general symmetry to the disturbing force to best attenuate acoustic radiation. Should the location of a vibration disturbance be unknown, the sensor and control force locations were also shown to prefer locations with moderate to high velocities and low

cross derivative. Additional simulation using fixed sensor and actuator locations indicated that SED-based control achieves similar attenuations to simple control of velocity at the same location, but typically causes less unwanted amplification. Control of velocity at both the SED sensor location and one additional location performs slightly better than SED-based control. SED-based ASAC may be a good option when a compact sensor is required. General interpretation of simulation results highlighted the importance of engaging multiple mechanisms of control simultaneously through both sensor and actuator selection and placement. This guideline should have application to other forms of active control.

3.3 Keywords

Active structural acoustic control, structural energy density, genetic algorithm, active noise control

3.4 Introduction

Active noise control (ANC) has been developed as a means of reducing unwanted noise for situations in which the use of passive materials is infeasible due to volume or weight restrictions. Active structural acoustic control (ASAC) is a specialization of ANC which can be used when the principal source of unwanted noise is a vibrating structure. The noise is managed through carefully devised control of the structural vibration. Everything from a single electromagnetic actuator [2] to arrays of actively controlled panels [17] have been employed to this end with varying degrees of success. While ASAC can eliminate noise at its source and has the advantage of compactness, it is often difficult to implement. Implementation is complicated by the interaction of the structure with its acoustic environment.

The treatment of complex systems is often made more practical through the use of energy-based methods. Two common examples are statistical energy analysis (SEA) and the use of the Euler-Lagrange equation in the analysis of dynamic systems. In each case, the use of energy-based methods improves utility by providing for practical comprehension of the critical features of an overall system while suppressing or decreasing sensitivity to excessively fine details.

One energy-based method with particular relevance to this work is energy-density-based active noise control (EDANC) [9]. Traditionally, ANC involves the minimization of squared sound pressure at one or more error sensors. The selection of the error sensor locations is often complicated by the existence of frequency-dependent pressure nulls. These cause a lack of correlation between the global acoustic response and what is measured at the error sensor. EDANC replaces the minimization of squared pressure with the minimization of the total acoustic energy, both potential and kinetic. Because of the complementary spatial relationship of the potential and kinetic energies, an acoustic energy density field has fewer nulls than a sound pressure field, and the effective volume of those nulls is significantly smaller for the energy density. EDANC is then able to provide better global sound attenuation in general than standard ANC with reduced sensor count and more flexibility in sensor placement.

The structural analogue of the acoustic energy density is the structural energy density (SED). It is comprised of terms related to kinetic and potential energies and strain as well as velocity. As an energy-based metric that incorporates multiple types of information, it may benefit ASAC in like manner to the application of acoustic energy density in ANC. Desired benefits include decreased sensitivity to sensor placement and improvement in global attenuation.

This paper is an investigation of the heretofore untested use of SED in active structural acoustic control. To that end, an assessment of the strengths, weaknesses, and practicality of the incorporation of SED into an ASAC system is presented. The scope of this research is limited to thin rectangular structures which radiate into free space or some other diffuse enviorment under the action of a single harmonic point force disturbance. Additionally, a control implementation involving a single point force actuator and a single SED sensor was assumed.

One additional energy-based metric related to structural vibration is the power flow or structural intensity. It has previously been used in control of structural vibrations, and relationships between power flow and acoustic intensity have been studied [18]. Previous work indicates that power flow can be difficult to reliably control due to multiple control solutions [19], and that it is not strongly correlated with the normal component of acoustic intensity [20]. For these reasons, power flow is not considered further in this work on energy-based ASAC.

As mentioned, the simulations presented in this paper relate to the use of SED-ASAC for free-field type applications. Simulations on the use of SED in controlling a panel radiating into a rectangular enclosure were commenced, but it became apparent that coupling between the panel and enclosure had a larger influence on the acoustic response than the placement of the SED sensor and control actuator. Effective control in such cases would require methods that explicitly consider the coupling relationships specific to the geometry of application [6, 21].

This paper is a substantial extension, correction, and clarification to [22].

3.5 Structural Energy Density

Structural energy density (SED) is a scalar quantity giving the combined potential and kinetic energy densities in a structure at a point. Timoshenko [23] gives expressions for kinetic and potential energy, the sum of which is the structural energy density. SED is calculated as

$$SED = \left(\frac{D}{2}\right)\left[\left(\frac{\partial^2 W}{\partial x^2}\right)^2 + \left(\frac{\partial^2 W}{\partial y^2}\right)^2 + 2\upsilon\left(\frac{\partial^2 W}{\partial x^2}\right)\left(\frac{\partial^2 W}{\partial y^2}\right) + 2(1-\upsilon)\left(\frac{\partial^2 W}{\partial x \partial y}\right)^2\right] + \left(\frac{\rho}{2}\right)\left(\frac{\partial W}{\partial t}\right)^2, \quad (3\text{-}1)$$

based on the complex displacement of the plate, W. The plate is described by its per-area mass ρ, thickness h, Poisson's ratio υ, and elastic modulus E. The bending stiffness of the plate is calculated as

$$D = \frac{Eh^3}{12\left(1-\nu^2\right)}. \quad (3\text{-}2)$$

Note that the absolute values of all partial derivatives are taken previous to performing any multiplication. Alternatively, the quantities can be left as complex values, with the complex conjugate of the second term being taken previous to multiplication. The term $\partial^2 W/\partial x \partial y$ will be hereafter referred to as the cross derivative, while $\partial^2 W/\partial x^2$ and $\partial^2 W/\partial y^2$ will be referred to as the non-mixed partials.

The terms within square brackets in Eq. 3-1 give the potential energy stored in the structure due to the interactions of the plate stiffness with the bending and twisting strains as calculated from plate displacement. The final term gives the kinetic energy associated with local plate velocity and per-area mass.

SED is not frequently referenced in ASAC literature, but has seen limited use in related work. Bouthier and Bernhard [24] developed energy transmission models based on SED as a facilitator for the study of passive structural acoustic control by damping treatments. Their work was primarily concerned with overcoming the limitations of modal analysis at mid to high frequencies in complex structures. Acoustic control was achieved by the distruption of vibrational energy transmission and structure-borne noise. Sakano and Tanaka [19] developed a method of active vibration control based on controlling the progressive waves in a structure. In

the course of their work they noted that as the progressive waves in a plate are controlled, the total vibrational energy in the entire plate decreases. This was an observational measurement of an area-integrated form of SED, and no attempt was made to control SED directly. Neither of these works provided any direct guidance on the relationships between SED and the acoustic response of a structure.

3.6 Mathematical Basis for Simulations

Before continuing with the investigation of SED-based ASAC, the structural and mathematical models shared in common by all simulations will be described. The structure simulated was a simply supported steel plate, with dimensions of 508 mm x 762 mm x 2 mm, corresponding to the variables a, b, and h, respectively. Properties given in accordance with the notation previously described are $E = 210\text{x}10^9$ Pa, $\upsilon = 0.29$, and $\rho = 15.6$ kg/m^2. The response of the plate at (x_m,y_m) to a point force of complex amplitude F and angular frequency ω located at (x_f, y_f) was calculated as

$$W = we^{j\omega t}, \tag{3-3}$$

in which the complex displacement amplitude w was determined using the modal representation given as

$$w(x_m, y_m) = \frac{4F}{ab\rho}\sum_{m,n}^{\infty} Q_{mn} \sin\left(\frac{m\pi x_m}{a}\right)\sin\left(\frac{n\pi y_m}{b}\right). \tag{3-4}$$

Q_{mn} gives the response amplitude at each of the contributing modes based on frequency, damping, and actuator position. It is calculated as

$$Q_{mn} = \sin\left(\frac{m\pi x_f}{a}\right)\sin\left(\frac{n\pi y_f}{b}\right)\left(\frac{\omega_{mn}{}^2 - \omega^2 - j\omega_{mn}{}^2}{\left(\omega_{mn}{}^2 - \omega^2\right)^2 + \left(\zeta\omega_{mn}{}^2\right)^2}\right), \tag{3-5}$$

the natural frequencies being given by

$$\omega_{mn} = \sqrt{\frac{D}{\rho}}\left(\left(\frac{m\pi}{a}\right)^2 + \left(\frac{n\pi}{b}\right)^2\right), \tag{3-6}$$

and a constant value of 0.001 being used for the damping factor, ζ.

This modal decomposition is based on that frequently used by Tanaka [19] with modifications to account for damping. SED can be calculated from the modal solution by taking appropriate spatial derivatives and making substitutions into Eq. 3-1. When taking derivatives, x_f and y_f are constants and x_m and y_m are the independent variables.

The objective of the simulations performed was to characterize general behavior and trends rather than make predictions with absolute accuracy. Thus, 400-500 total modes were used when obtaining the displacement response to avoid excessive computational times.

The complex pressure field p associated with the vibration-induced radiation of the plate into free space was approximated numerically by treating each element of the plate as a simple source and applying

$$p = \frac{j\omega\rho_o}{2\pi}\sum_i V_i \frac{e^{-jkR_i}}{R_i} A_i \,. \tag{3-7}$$

The expression for Rayleigh's integral found in [25] was discretized to obtain this equation. In addition to the variables previously defined, ρ_o is the density of air, V_i is the complex amplitude of the normal velocity of the plate at the i^{th} position, k is the acoustic wavenumber, R_i is the absolute distance from the i^{th} position on the plate to the acoustic measurement location, and Ai is the area of an individual element. The normal velocity was calculated by taking the time derivative of the complex plate displacement solution. This was trivially obtained by multiplying the complex displacement by $j\omega$.

The simulations performed also required a measure of acoustic intensity, which was calculated based on a central-difference approximation using the pressure estimates surrounding the point of interest. Mathematically, this is expressed as

$$\vec{I}(x,y,z) = \frac{1}{2\rho_o \omega} \begin{Bmatrix} (p(x+\Delta x))^* (p(x-\Delta x))/\Delta x \\ (p(y+\Delta y))^* (p(y-\Delta y))/\Delta y \\ (p(z+\Delta z))^* (p(z-\Delta z))/\Delta z \end{Bmatrix}. \tag{3-8}$$

In addition to the notation previously used, Δx , Δy, and Δz are the finite-difference spatial step sizes. The * denotes a complex conjugate.

3.7 Control Suitability of Structural Energy Density

As SED has seen very little if any use in active control, it is worth investigating its suitability for incorporation into an active control system. If SED cannot be robustly measured and minimized, SED-based ANC will be of no utility. To this end, two questions are addressed by means of simulation.

First, is the mathematical space in which SED resides amenable to gradient-based optimization? Problems such as poorly shaped contours and multiple minima would indicate slow convergence and unpredictable results in real-life active control implementation. To answer this question, simulations were performed in which the plate was subjected to a unit disturbance force and a non-collocated varying control force while SED was calculated at a sensor location. The disturbance force complex amplitude was held constant while the real and imaginary gains of the control force were varied between -4 and +4. The SED amplitude was calculated for each complex gain and the results were used to characterize the minimization space in which SED resides.

The minimization space of SED was found to be well suited to standard control methods such as steepest descent and filtered-X type algorithms. For example, the space always includes a single minimum. Additionally, the contours of SED indicate that this minimum resides at the bottom of an elliptically shaped bowl. This indicates that a single control solution exists, and that convergence can theoretically be achieved regardless of the initialization of the control coefficients.

The only difficulty indicated by the shape of the SED minimization space is related to the gradients near the minimum. Because these are small, the region of the complex gain domain that is within the noise floor of the control system hardware and software is larger than it would be if the gradient was steeper. Depending on the noise floor and precision of the components used, this could be a problem.

The second question related to control suitability is this: How does the placement of a sensor on the structure affect the quantity measured? If the mass-loading of a sensor has little effect on SED, the control system will be easier to design, and more of the control effort will be used to achieve actual control objectives. If the mass loading has a large effect, the control system will be more difficult to design because it will require joint and likely iterative characterization of the structure-sensor system. While sensor mass loading does not typically seriously affect a heavy structure, many structures of interest in ASAC are made of sheet metal or other lightweight material. Consideration of mass loading will help to clarify the applicable scope of SED-based ASAC techniques.

To answer this second question, the SED profile of the simulated plate under the action of a disturbance force was calculated. A second reactive force due to the acceleration of a small

point mass affixed to the plate was then determined. The complex amplitude of the reactive force was calculated by applying Newton's second law. This was implemented as follows: the combined effect of the disturbing and reactive forces was required to cause an acceleration of the affixed mass that would produce the same reactive force as was applied to the plate. When the reactive force had been determined, the SED profile of the plate under the simultaneous action of both forces was calculated and compared with the original profile. Note that SED cannot be obtained by superposition of the SED fields of individual responses because of quadratic terms. The simulation described was performed at various frequencies. The results of one of many possible examples are presented.

Figure 3-1 shows the SED profile in the plate at 94.5 Hz (near the 1-3 mode at 95.4 Hz) due only to a unit disturbance force applied at (*a/5, b/5*). A 0.010 kg mass loading was then applied at (*3a/5, 4b/5*), and the associated reactive force was calculated. Figure 3-2 shows the SED profile due to the combined effect of the disturbance and reactive forces.

With the addition of mass loading, the SED amplitude approximately doubles. However, there is very little change in the spatial distribution. These effects were investigated at many frequencies and it was found that the spatial distribution of SED is robust against mass loading effects, while the SED amplitude levels are only slightly affected except at frequencies near the natural frequencies of the plate. This indicates that an SED-based control system could be installed without too seriously disturbing the quantity it attempts to control. Note that the simulation performed here uses a simplified representation of the SED sensor by treating it as a point mass rather than a compact array of discrete sensors.

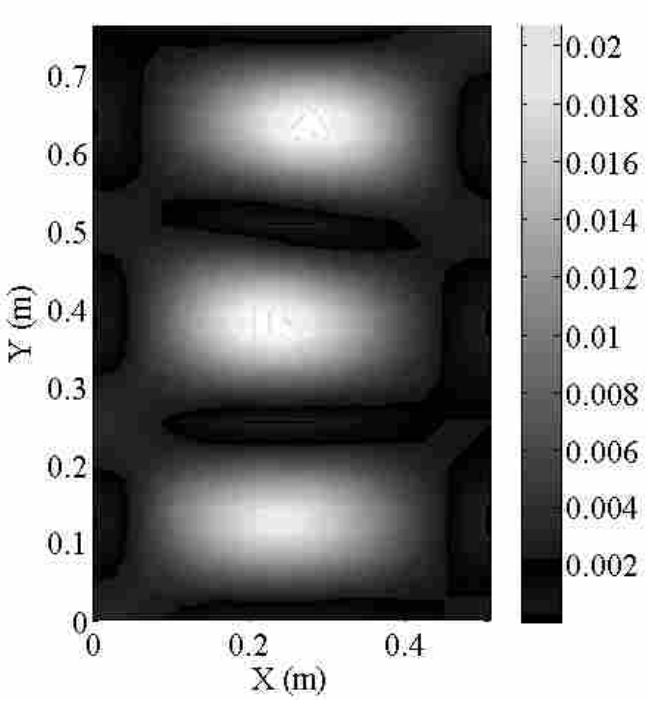

Figure 3-1: SED Before Mass Loading (J/m^2)

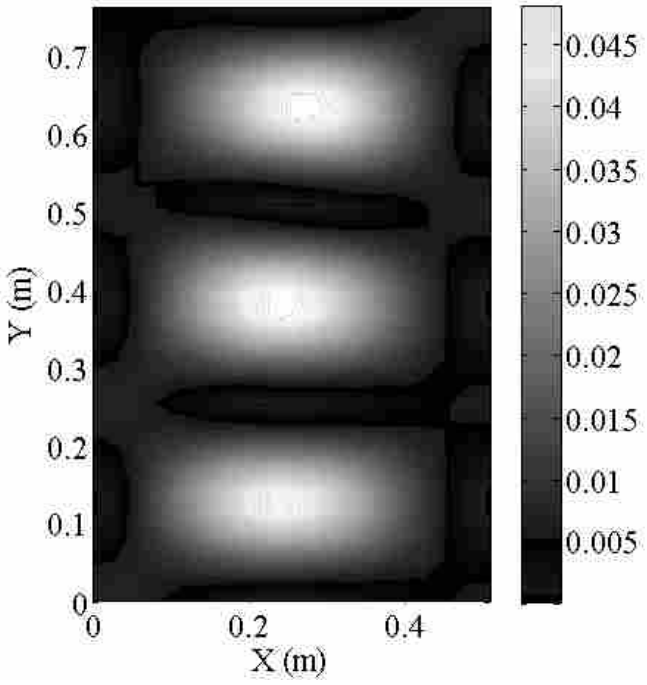

Figure 3-2: SED After Mass Loading (J/m^2)

3.8 Genetic Optimization of Control System Design

With the practicability of SED control having been demonstrated, a second set of simulations is presented in which a genetic algorithm was used to extract design guidelines for optimal sensor and actuator placement of an SED-based ASAC system. It was also hoped that interpretation of the results would provide insight into the relationship between SED and the acoustic response. The premise of these simulations is as follows: The simply supported steel plate described in Section 3.6 radiates into free space, being disturbed by a single point force of unit amplitude at a single frequency. An actively controlled point force also excites the plate, with a single sensor measuring SED at some location on the plate.

The genetic algorithm was designed to select locations for the control force and SED sensor such that as SED at the sensor location was minimized, acoustic radiation away from the plate was also minimized. Equation 3-8 was used to calculate an intensity vector at 925 evenly spaced points on a plane 7.5 cm above the plate which extended 8 cm beyond the plate boundaries in each direction, based on complex pressures calculated on planes 5 cm, 7.5 cm, and 10 cm above the plate. Energy transfer was approximated as the absolute value of the mean intensity vector. This absolute-mean-vector intensity will hereafter be referred to simply as intensity level unless otherwise noted.

To achieve the desired minimization of intensity level, the genetic algorithm optimized a chromosome of four genes which described the x and y positions of the control force and SED sensor. The sensor and actuator were permitted to be located anywhere on the plate except for a 5 cm strip around all edges. The population typically included 20-30 individuals, with approximately 40 generations being allowed for the population to evolve. Tournament selection

was used, with the tournament size being approximately 40% of the population size. Children were required to compete with parents in order to become part of the next generation.

The randomly created initial generation was typically composed of a large number of comparably poor designs and one or two highly superior designs. This made the achievement of diversity in the population and thus improvement in design a substantial challenge. To this end, high mutation and crossover rates of 0.1 and 0.4 respectively were employed. An additional condition was also added in which "twin" designs were eliminated by allowing only one of multiple instances of an identical chromosome to advance to the next generation. Without this condition, the population was very quickly dominated by a single design and improvement ceased. Competition between parents and children prevented the high mutation and crossover from eliminating or corrupting the best designs.

Fitness was assigned to each individual according to the intensity level after minimization of SED by a control system having sensor and actuator locations described by the chromosome for that individual. An important intermediate step in the calculation of fitness was the determination of the control force complex gain which resulted in minimization of SED. The complex gain could have been found using any one of many existing search and optimization methods. The method chosen was a variation of the bisection method. Minimization of SED was not found to require excessive control force, and therefore no restrictions were placed on complex gain amplitude during evaluation of fitness.

As every physical sensing and control system has a noise floor beyond which it will not be possible to minimize the measured quantity, the true objective of this simulation was to find the design with the best minimization efficiency. In other words, a set amount of minimization of SED should result in the maximum reduction of intensity level. One method of simulating a

noise floor is to add random noise to the SED sensor "signal". However, this would have made fitness calculations inconsistent and unrepeatable. Rather than adding random noise, the noise floor condition was implemented by not allowing the intermediate minimization to reduce SED to less than 2% of its global maximum uncontrolled value.

Three types of descriptors were used in analyzing the optimized results. The first is related to the plate geometry. Sensor and actuators were described by physical location as a percentage of the plate dimensions.

The second type of descriptor is based on the idea that at modal frequencies, the behavior of the structure at any point will be very similar to its behavior at any other point which has the same relative proximity to nodes and antinodes. Mathematically, this was computed by assigning each point a value between 0 and 1 in each dimension. A value of 0 would indicate the sensor was placed on one of the nominal nodal lines of the plate, while a value of 1 would indicate it was placed at a nominal antinode. These values are referred to as mode-normalized coordinates, and were only applied to the simulations of Section 3.8.1.

The third type of descriptor is based on the idea that in order to minimize radiation, the SED sensor is driven to a location with the right contributions from the five subcomponents in the SED equation. Four of the subcomponents are products of three spatial derivatives of displacement, the fifth is simply the velocity. At near-mode frequencies the structural response is dominated by a single mode and the spatial distribution of the velocity is nearly identical to the spatial distribution of the non-mixed partial derivatives. Thus, subcomponent targeting for modal frequencies can be adequately described by only giving levels of the velocity and cross derivative at the optimized sensor location relative to their uncontrolled spatial maximums. Note that these descriptors can take on values greater than 100%. The uncontrolled spatial maximums

were estimated from the collection of response values which had already been calculated at each of the plate elements used in approximating Rayleigh's integral. Because the genetic algorithm could place sensors and actuators in continuous space, it occasionally chose locations with higher values than were found at any of the discrete elements.

Using the methods described, two rounds of simulation were performed. The first round considered behavior at the first 16 structural modes of the plate. The second round operated on frequencies uniformly spaced from 20 to 200 Hz.

3.8.1 Modal Frequency Simulations

The genetic algorithm was first applied at modal frequencies. Table 3-1 lists the first 16 modes and their corresponding frequencies. For the (*m,n*) mode, the unit disturbance force was applied at (*a/2m, b/2n*) to give optimal structural disturbance excitation. Optimization was performed four times at each frequency to verify consistency and allow for averaging of results.

Table 3-1: Modes and Frequencies for the First Round Optimization

Mode	*Frequency (Hz)*
(1,1)	27.52
(1,2)	52.93
(2,1)	84.68
(1,3)	95.27
(2,2)	110.09
(2,3)	152.43
(1,4)	154.54
(3,1)	179.95
(3,2)	205.35
(2,4)	211.70
(1,5)	230.76
(3,3)	247.69
(2,5)	287.92
(3,4)	306.97
(4,1)	313.23
(1,6)	323.91

The optimized control system designs were able to attenuate radiation at all modal frequencies studied. The attenuation levels indicated that at modal frequencies, SED amplitude at the optimized sensor locations is a good predictor of intensity level. This was demonstrated by a consistent 17 ± 0.3 dB average reduction in intensity level, which matches the 17 dB maximum allowed reduction in SED imposed by the noise-floor constraint of the genetic algorithm.

Optimized SED sensor placements were spread over most of the plate. Analysis by physical location did not yield strong trends. However, from a visual inspection of the data it was apparent that the locations were not random. Sensor placements were generally clustered together in one or two small groups at any given frequency.

Mode-normalized coordinates were subsequently calculated for each optimized design and then averaged by frequency. The results are presented in Table 3-2. As can be seen, the sensor placement was driven to locations at or near the nominal antinodes of the plate.

Table 3-2: Average Optimized Mode-Normalized Sensor Location Coordinates, First Round

Mode	*Mode-Normalized x*	*Mode-Normalized y*
(1,1)	1.00	0.99
(1,2)	0.99	0.99
(2,1)	1.00	0.98
(1,3)	0.98	0.97
(2,2)	0.98	0.98
(2,3)	0.98	0.99
(1,4)	0.99	0.99
(3,1)	0.98	0.98
(3,2)	0.98	0.98
(2,4)	0.98	0.99
(1,5)	0.98	0.94
(3,3)	0.96	0.96
(2,5)	0.99	0.97
(3,4)	0.97	0.99
(4,1)	0.99	0.98
(1,6)	0.97	0.99

Analysis of sensor location according to the contributions of the subcomponents of SED was also performed. Table 3-3 gives information on the average velocity and cross-derivative levels at the SED sensor as compared to the estimated uncontrolled spatial maximum values of those quantities. Sensor placement consistently coincided with regions of high velocity and lower cross derivative.

Table 3-3: Average Velocity and Cross Derivative Levels at Optimized Sensor Locations, First Round

Mode	*Percentage of maximum velocity*	*Percentage of maximum cross derivative*
(1,1)	100	0
(1,2)	100	0
(2,1)	102	0
(1,3)	101	0
(2,2)	102	0
(2,3)	103	1
(1,4)	100	0
(3,1)	100	0
(3,2)	100	0
(2,4)	102	0
(1,5)	100	0
(3,3)	101	0
(2,5)	102	0
(3,4)	100	0
(4,1)	102	0
(1,6)	101	0

The position descriptors presented in the preceding tables indicate that at modal frequencies with optimum structural excitation, sensor placement should coincide with antinodes. For fixed sensor placement, the most efficiently radiating odd-odd modes all share an antinode at the center of the panel. The results also indicate that the sensor is driven to locations of high velocity and non-mixed partials and low cross derivative. The correlation between these is natural; at modal frequencies, locations of very low cross derivative are coincident with

locations of very high velocity and non-mixed partial derivatives, and are also coincident with the antinodes. Because of the strong spatial relationships between all aspects of the structural response at modal frequencies, it is not possible at this point to determine if velocity level, non-mixed partial derivative level, or near-antinode location is the best predictor for effective sensor placement.

Actuator location results from the first round of genetic optimizations will now be considered. Optimized actuator locations did not show the same repeatability as sensor location. Although grouping was weak, some trends were still apparent in the results. In this case, analysis of geometric position and levels of the SED subcomponents proved more useful than mode-normalized coordinates. As the data are best suited to visual interpretation, results are presented in histogram form rather than tables.

The geometric distribution of the control force location is shown in Figs. 3-3 and 3-4. Position was converted from geometric length to a percentage of each plate dimension. From these plots, it is apparent that the control force location tends slightly towards locations at the upper right corner of the plate. As previously explained, the disturbance force was applied at the nominal antinode nearest the lower-left corner of the plate at each frequency. The tendency of the control force to take a position opposite that of the disturbance force indicates that the control force placement may be influenced by a preference for symmetry or remoteness relative to the disturbance force location, or possibly both. The lack of actuator locations near the edges of the plate is a result of restriction on the domain rather than an optimization result. This restriction was intended to prevent actuator locations that would require excessive force, and sensor locations at which there would be little SED to measure.

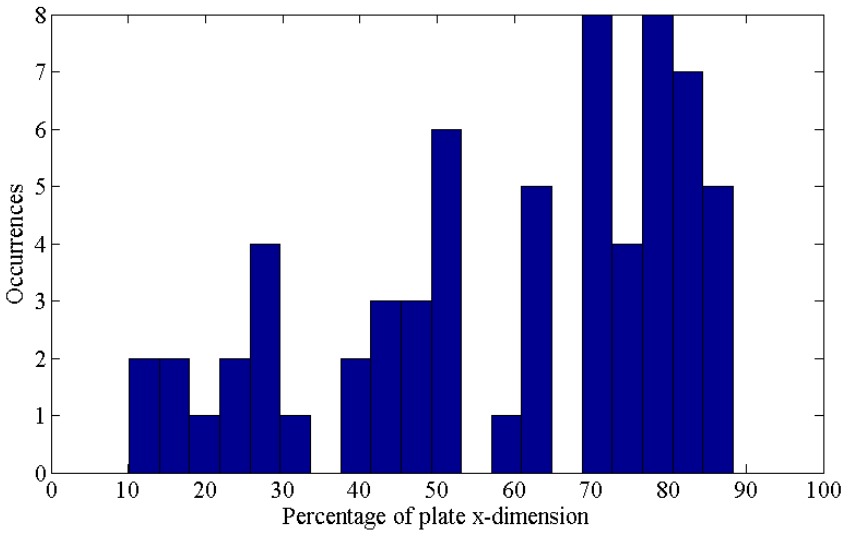

Figure 3-3: Distribution of Optimized Actuator x-Positions, First Round

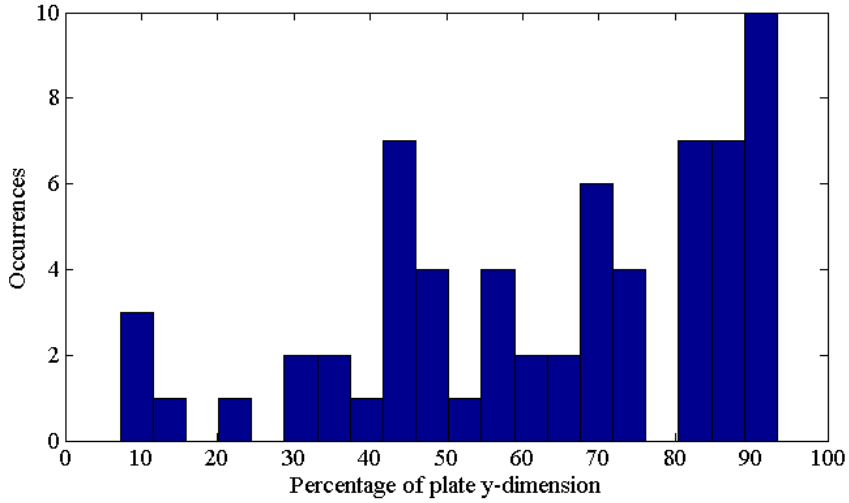

Figure 3-4: Distribution of Optimized Actuator y-Positions, First Round

The distribution of control force locations as a function of the levels of the subcomponents of SED at the actuator position, and as selected by the genetic algorithm is shown in Figs. 3-5 and 3-6. The control force location does not appear to be highly correlated with the velocity level at the forcing location. It is apparent, however, that it should be placed at locations with lower cross-derivative levels. This finding may be more related to the use of a

point-force actuator than the use of SED-based control. Regions of high cross derivative are associated with corners of the plate and the intersection of nodal lines. A point force actuator would have difficulty coupling with the structure at such locations.

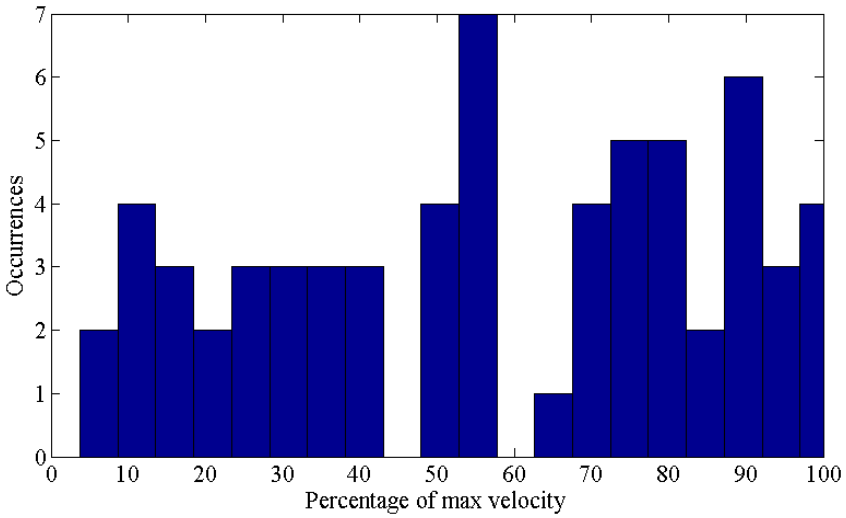

Figure 3-5: Distribution of Optimized Actuator Locations According to Velocity at the Actuator, First Round

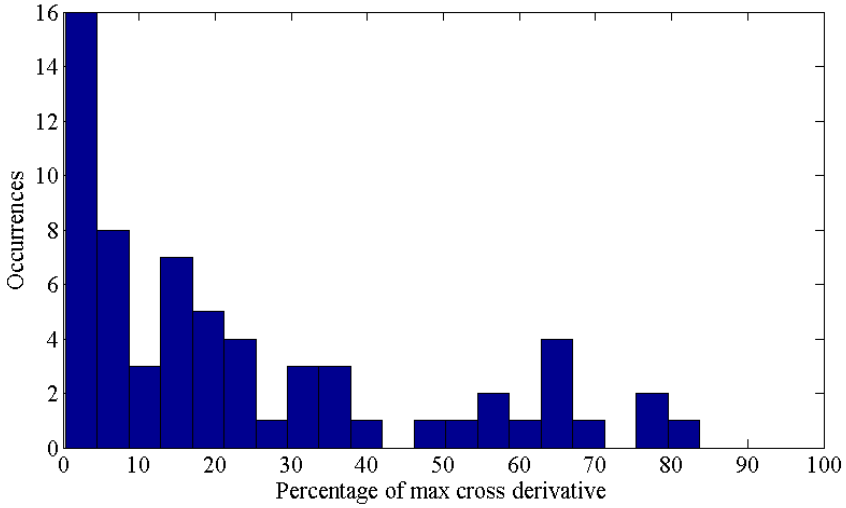

Figure 3-6: Distribution of Optimized Actuator Locations According to Cross Derivative at the Actuator, First Round

The results of the modal optimization assigned more importance to the sensor location than the actuator location. It was apparent that both sensor and actuator should avoid regions of high cross-derivative, but due to confounding effects, it was not apparent if the levels of velocity or the non-mixed partial derivative subcomponents of SED are a better predictor for sensor placement. A second set of genetic optimizations was performed.

3.8.2 Uniformly Spaced Frequency Simulation

The second round of simulations utilized the same simply supported plate and genetic algorithm as the first, but frequencies were evenly spaced from 20 to 200 Hz in 3 Hz increments. In addition, the disturbance force was applied at (*a/3, b/3*) for all frequencies rather than being constantly shifted to the lower leftmost antinode.

Four optimization runs were performed at each frequency, with the resulting average intensity level relative to the uncontrolled level being shown in Fig. 3-7. Although the noise-floor condition remained active, the attenuations in acoustic radiation varied significantly with frequency. Performance was generally better at lower frequencies, especially at frequencies near the fundamental structural mode.

The worst performance coincided with frequencies near 95 and 180 Hz, which correspond to the (1,3) and (3,1) modes respectively. For such cases, the disturbing force location coincided with a nodal line of the dominant structural mode, resulting in minimal excitation. If the control force were also located on a nodal line, it would not be able to effectively couple and control SED. Unfortunately, by placing the control force away from the nodal line, it is likely to create spatial spillover, exciting the dominant structural mode and thereby possibly increasing acoustic radiation. It is hypothesized that the optimization of these competing objectives resulted in the poor performance shown.

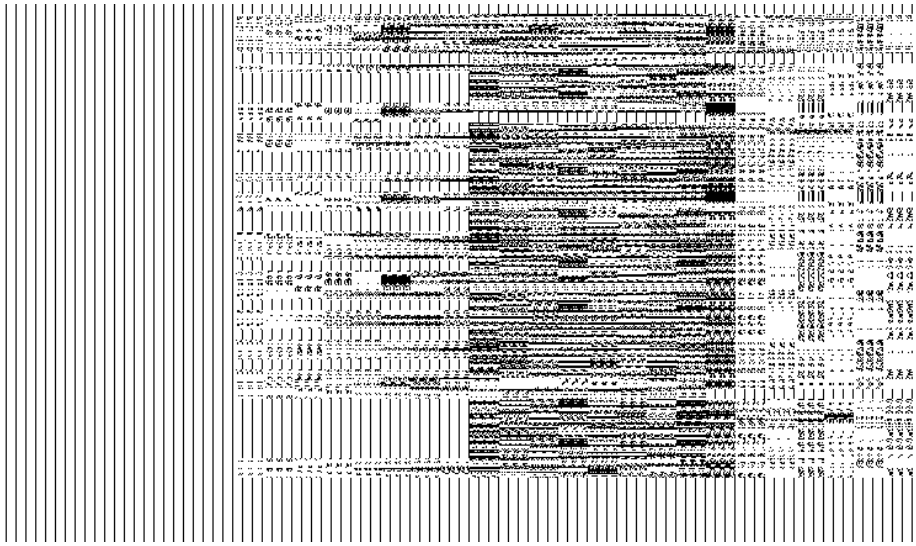

Figure 3-7: Average Optimally Controlled Intensity Level Relative to Uncontrolled Intensity Level, Second Round

While the first set of simulations showed very consistent sensor placement and varied force placement, the second set of simulation results had the opposite trends. Nevertheless, a substantial amount of cross-validation is found in the results. As most frequencies did not coincide with structural modes, mode-normalization of coordinates was not used to analyze the results. However, analysis of SED subcomponent levels was instructively applied. Results for sensor placement are presented first, followed by results for control force location.

The optimized geometric x and y locations for the sensor are shown in Figs. 3-8 and 3-9 respectively. With the disturbance force location fixed, the sensor location was also much more consistent geometrically. Both *x* and *y* positions show a preference for locations that are somewhat symmetric to the disturbance force in either the *x* direction, *y* direction or both. There is also a slight drift towards the edges of the plate. Although not immediately apparent, the first set of simulations also indicated that the sensor should have some symmetric relationship to the disturbance force. In that case, the disturbance force and SED sensor were both located at

antinodes. Although two antinodes may not have symmetry with respect to the plate geometry, they may be considered symmetric in a general sense due to the repetition of modal patterns.

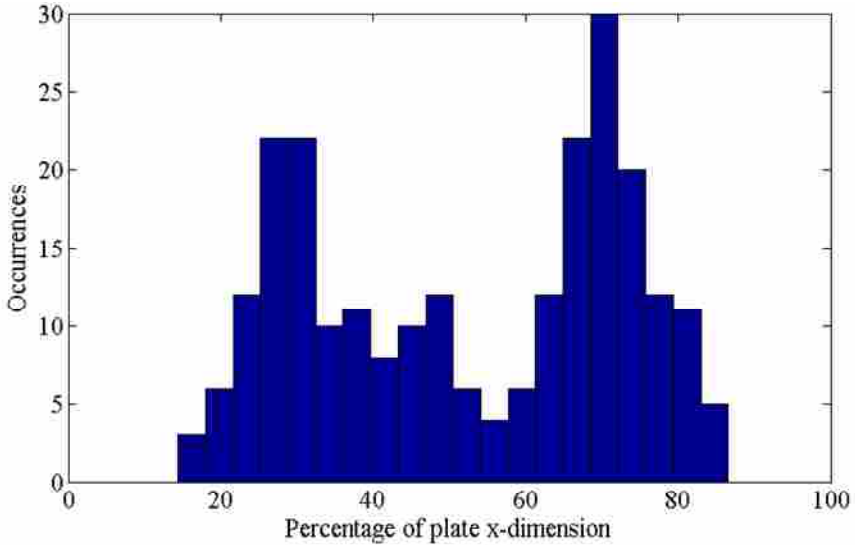

Figure 3-8: Distribution of Optimized Sensor x-Positions, Second Round

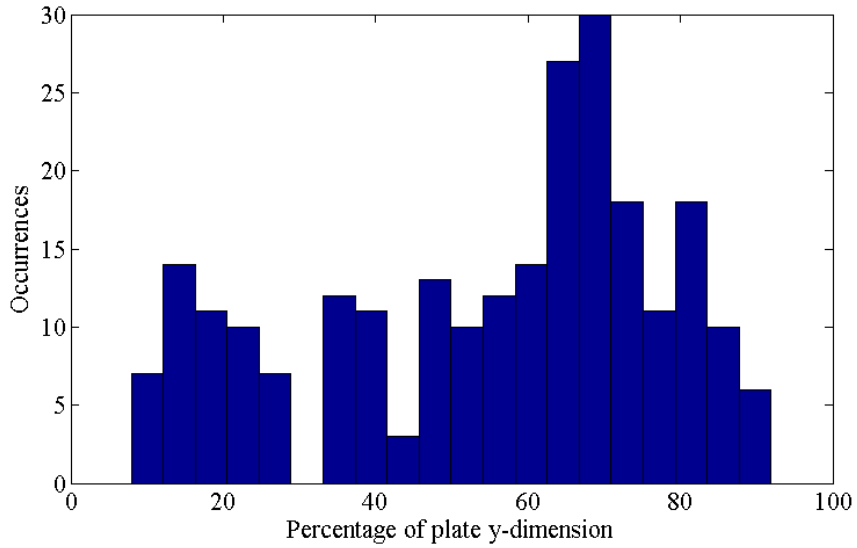

Figure 3-9: Distribution of Optimized Sensor y-Positions, Second Round

SED component-based normalization was also performed. Results again showed that the sensor should be placed at locations of higher velocity and low cross derivative as shown in Figs. 3-10 and 3-11, although the grouping was not as pronounced as in the first round simulations.

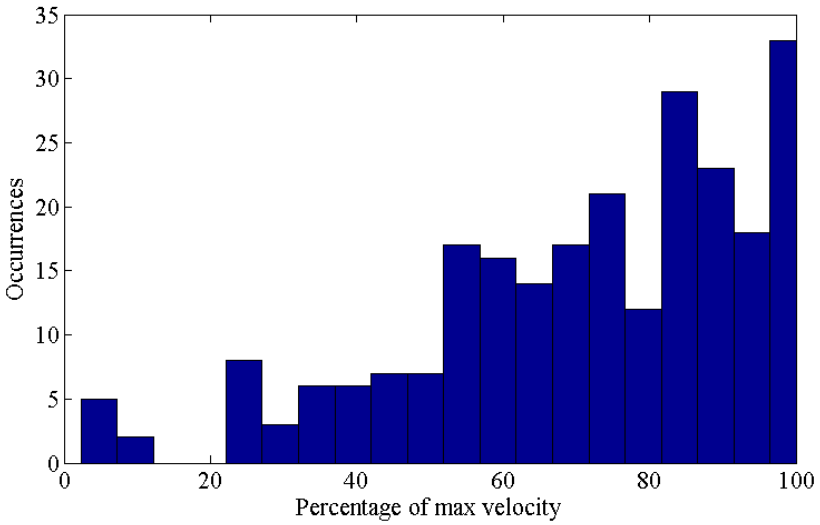

Figure 3-10: Distribution of Optimized Sensor Locations According to Velocity at the Sensor, Second Round

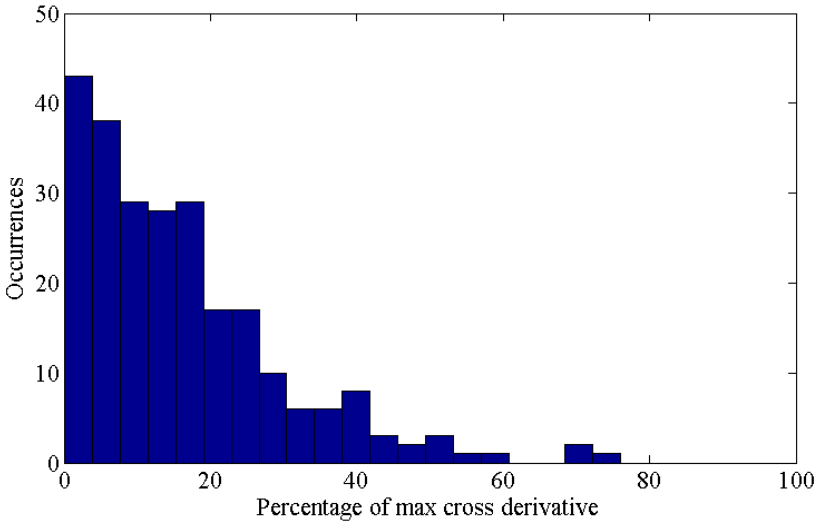

Figure 3-11: Distribution of Optimized Sensor Locations According to Cross-Derivative at the Sensor, Second Round

For the uniformly spaced frequencies simulated, the spatial distributions of the velocity and non-mixed partial derivatives are not identical. The results relating sensor placement to the non-mixed partials were therefore calculated. The sensor placement covered the entire range of the non-mixed *x* derivative, with a slight bias towards higher values. The non-mixed *y* derivative was also quite spread out, but had a noticeable concentration around 50%-70% of the maximum. These trends were less strongly defined than those seen in Figs. 3-10 and 3-11, which may indicate that velocity should be considered first when placing sensors.

The location of the control force is now considered. Figures 3-12 and 3-13 show the distribution of geometric x and y positions respectively of the optimized control force locations. These are clustered around the location (*2a/3, 2b/3*) which is symmetrically opposite the disturbing force. This symmetry effect was weakly present in the modal simulations, but it is observed here to a much higher degree.

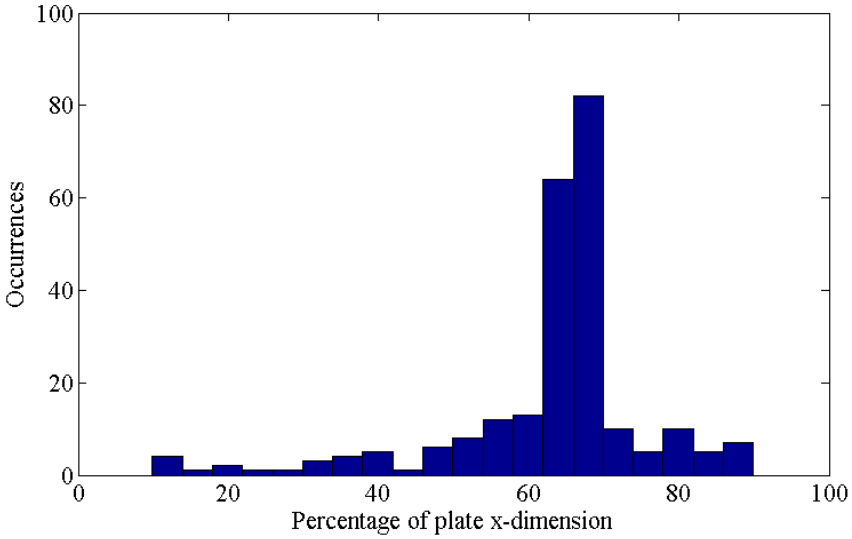

Figure 3-12: Distribution of Optimized Actuator x-Positions, Second Round

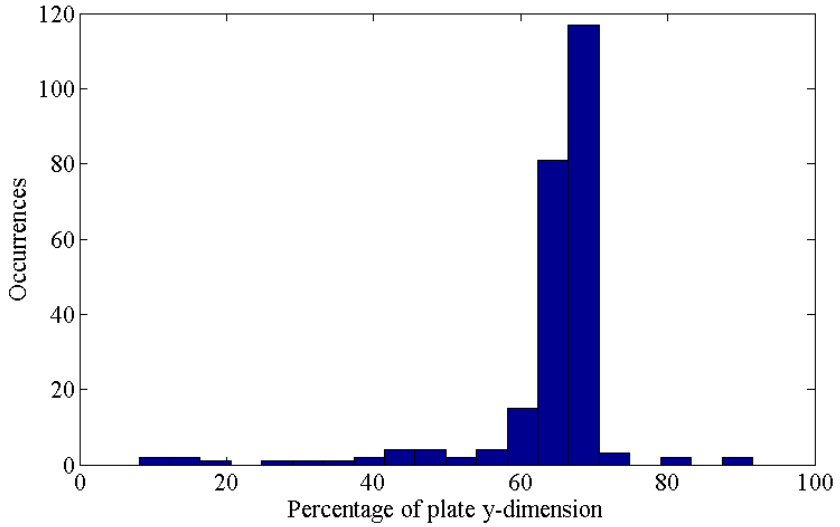

Figure 3-13: Distribution of Optimized Actuator y-Positions, Second Round

Figures 3-14 and 3-15 show the distributions of normalized velocity and cross-derivative levels respectively at the optimized actuator locations. As in the first round of simulations, velocity is not a strong driving parameter for control force placement. A preference remains for locations with low cross derivative, but the effect is less pronounced.

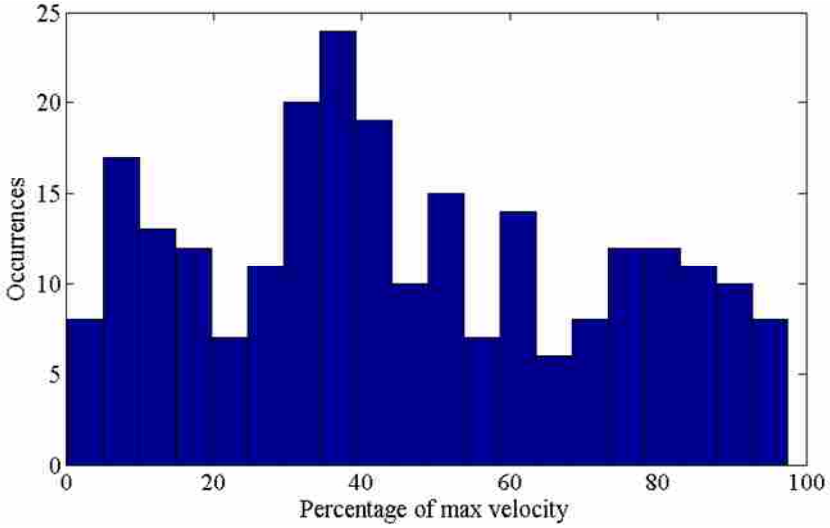

Figure 3-14: Distribution of Optimized Actuator Locations According to Velocity at the Actuator, Second Round

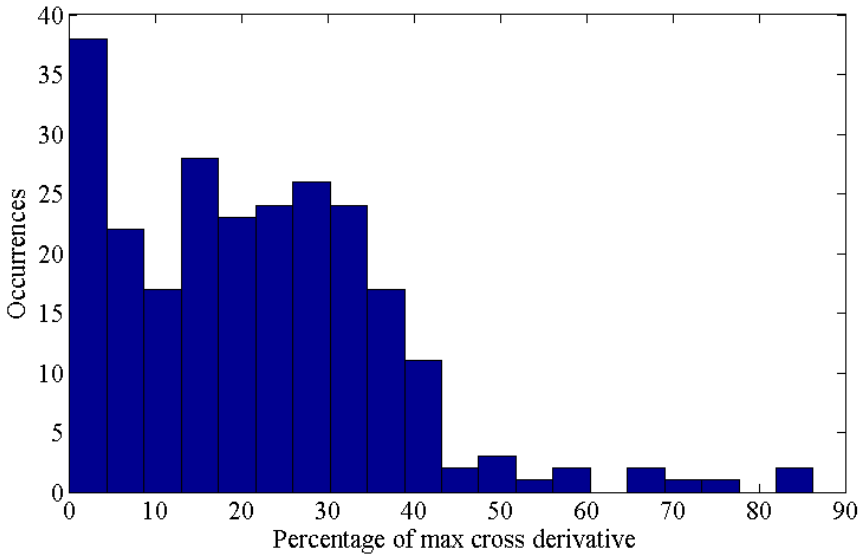

Figure 3-15: Distribution of Optimized Actuator Locations According to Cross-Derivative at the Actuator, Second Round

As with sensor position, the control force position was also described by normalized levels of the non-mixed partials. The resulting distributions were relatively uniform, with a slight bias towards lower values. The distributions were not deemed informative enough to justify including plots.

Both genetic simulations indicated two possible influences in sensor placement. The first is the uncontrolled structural velocity at the sensor location, which tended towards higher values. The second is symmetry relative to the disturbing force. Symmetry related to both geometric location and antinode similarity was observed in the results. If velocity should be the overriding predictor of the performance of an SED-based ASAC system, then control of SED would be nothing more than velocity control with a more complicated implementation, and marginal performance would be expected.

3.9 Comparative Fixed-Design Simulations

To further explore the velocity and symmetry influences suggested by the genetic algorithm results, two simulations were performed which compared three types of control: SED control, single point velocity control, and two-point velocity control. Control was simulated at frequencies from 20 to 200 Hz in 1 Hz steps. The fitness function of the genetic algorithm was used to calculate the intensity level at each frequency. The noise floor condition used in the genetic algorithm was not imposed for these simulations because the objective was to compare performance rather than efficiency.

The first of these simulations was designed under the assumption that velocity is the determining factor in sensor placement. A unit disturbance force was applied to the plate at (*3a/10, 3b/10*). The control force was applied at (*4a/5, 4b/5*) so as to be located nearly, but not perfectly symmetrically to the disturbance. This placement reflects the need for symmetry indicated by the second set of genetic algorithm simulations, as well as the preference for locations farther from the disturbing force as indicated by the first set of genetic algorithm simulations. The SED sensor was located at (*a/2, b/2*), that being a location of high velocity for the most efficiently radiating modes. Velocity sensor 1 was collocated with the SED sensor to provide for direct comparison of SED-based and velocity-based control. Velocity sensor 2 was located at (*3a/4, b/4*) after some experimentation to determine a location which subjectively effected the most improvement over using only velocity sensor 1.

Figure 3-16 shows the intensity level for the three types of control, as referenced to the uncontrolled intensity level. As can be seen, SED control had nearly identical performance to single-point velocity control below 90 Hz, and superior performance in the higher end of the frequency range studied. Two-point velocity control was comparable or superior to both SED

and single-point velocity control at most frequencies. Although SED-control appears to offer some improvement over velocity control, it also suffers from some of the same weaknesses. For example, in the 40-90 Hz range, the structural response is dominated by the (1,2) and (2,1) modes, neither of which is highly observable at the center of the plate for either velocity or SED sensors.

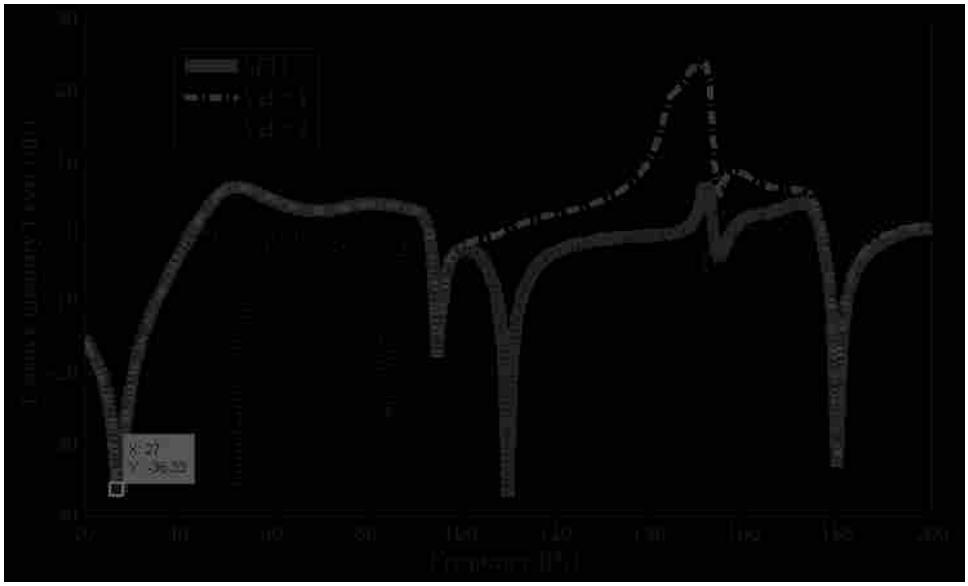

Figure 3-16: Comparison of Three Types of Control When Velocity Level is Given Preference in System Design

The second simulation on comparative control was designed to test the importance of placing the sensor at locations of symmetry relative to the disturbance force. To this end, the SED sensor was moved to (*4a/5, 4b/5*), making it collocated with the control force and giving it the same imperfect symmetry. The intensity levels for the three types of control as compared to the uncontrolled level are shown in Fig. 3-17.

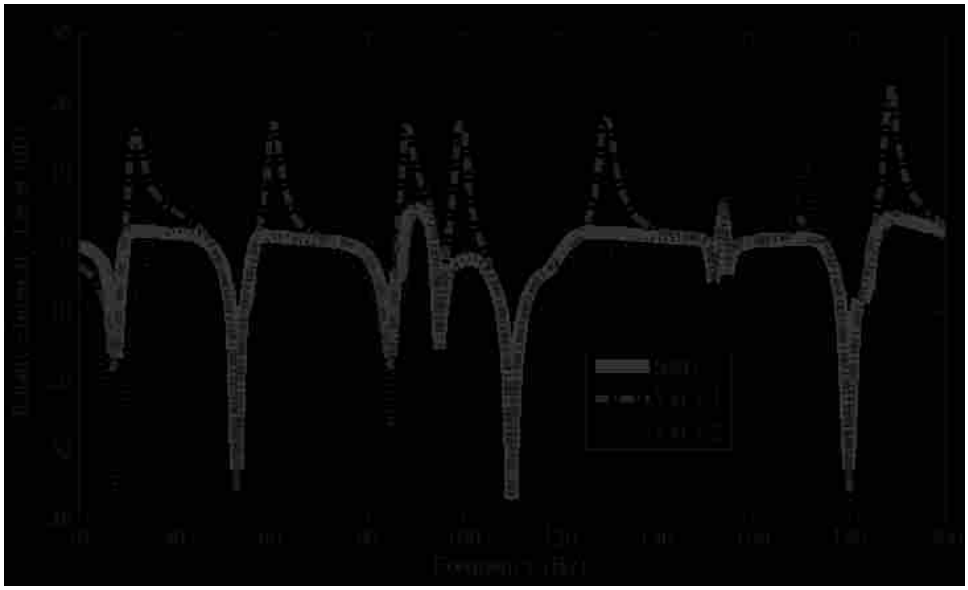

Figure 3-17: Comparison of Three Types of Control When Velocity Level is Given Preference in System Design

The results presented in Fig. 3-17 show similar behavior to the previous experiment. SED-based and single-point velocity control achieve comparable maximum attenuations. The performance of both methods is still exceeded by two-point velocity control, although less so for SED-based control. The most substantial change affected by a switch to symmetric sensor placement is that SED-based control is much less prone to causing unwanted amplifications. It was also able to provide attenuation in the 40-90 Hz range through improved observeability.

From these simulations, it appears that SED control is generally more effective than velocity control at the same location, and that symmetry to the disturbance force is a better general criterion for SED sensor placement than velocity level. The only frequency at which performance of the SED-based system decreased due to a switch to symmetric sensor placement was at the fundamental mode of the plate. Attenuation in intensity level was decreased from approximately 37 to 17 dB. Departure from the symmetry guideline would only be advisable for

applications in which the frequency content of the disturbance was concentrated near the fundamental frequency of the structure.

With sensor-actuator collocation and symmetry relative to the disturbance, SED-based control provides very comparable performance to two-point velocity control at most frequencies. Simulations using three and four point velocity control did not affect substantial improvements over two-point control. SED-based ASAC may therefore be a good option when for accessibility or aesthetic reasons, the control system is limited to a single compact sensor.

Unfortunately, while SED-based ASAC functions well at single frequencies with proper system design, it does not achieve the desired decrease in sensitivity to sensor placement observed in its acoustic analogue, EDANC. Sensitivity to sensor placement is highlighted by the differences in Figs. 3-16 and 3-17. Part of the reason for not achieving decreased sensitivity may be that the observability of SED is not uniform across the plate. As noted in Section 3.8, the velocity and non-mixed partial derivatives in SED have the same spatial distribution. This distribution has maxima at antinodes, and nulls at nodal lines. The spatial distribution of the cross derivative has maxima at the intersection of nodal lines, and nulls at the antinodes. Although the cross derivative reduces the area of SED nulls on the plate, genetic simulation indicated that minimization of the cross derivative is much less important in reducing radiation than minimization of the velocity and non-mixed partials. In light of this, the effective null area on the plate is no better for SED-based control than for velocity-based control.

3.10 Additional Interpretation of Results

This section contains a brief commentary on how the simulation results presented may have application to other forms of ASAC.

It is worth considering why the control force was driven by the genetic algorithm to locations of symmetry and remoteness relative to the disturbance force rather than being collocated with it. No effort was made to prevent collocation, and such an arrangement would allow for direct reduction of the amplitude of both structural and acoustic responses. A likely explanation is related to the work of Fuller *et al*. [26] who noted that a structural actuator has two operating paradigms for reducing radiation. The first is to reduce the overall vibration amplitude. The second is to reshape the structural response so that it radiates less efficiently. He indicated that the first operating paradigm was dominant at modal frequencies, and the second was dominant at off-modes. This paper proposes that both can be active simultaneously.

Simultaneous operation of both reduction mechanisms is achieved through symmetric placement of the control actuator as follows. First, with symmetric placement, the control actuator has comparable input impedance to the disturbing actuation and thus equal control over vibration amplitude. Second, symmetric placement puts opposing forces in diagonally opposite corners of the plate. This condition has an even character that in general does not promote efficient acoustic radiation.

The simultaneous operation of both control mechanisms does not provide a means of increasing the theoretical achievable attenuation but does provide a means of increasing the efficiency of control. In theory, complete attenuation of the structural and acoustic responses could be achieved in an ideal system by collocating the control and disturbance actuators and minimizing any aspect of the structural response at any location on the structure. Had the genetic algorithm been run without a noise floor constraint, this would most likely have been the outcome. However, because the algorithm was not allowed to entirely eliminate the structural

response, it was forced to seek the most efficient locations for the sensor and control force, and thus selected a location that utilized dual modes of control.

As all real active control systems are limited by a noise floor, the results obtained here by study of SED-based ASAC suggest the following general guideline. The placement of actuators for any type of ASAC should be such that they have the capability to reshape the structural response in addition to attenuating it.

A similar concept can be developed with regards to sensor placement. SED includes terms which depend on velocity, and terms which depend on the spatial derivatives of displacement. All simulations indicated that minimization of the cross derivative is not a significant contributor in reduction acoustic radiation. The question then remains, "Is minimization of velocity or the non-mixed partials more important for achieving acoustic attenuation?"

The first round of genetic simulations did not answer this question because the spatial distributions of the velocity and non-mixed partials were nearly identical. Minimization of one resulted in minimization of the other as a natural byproduct. The second round of genetic simulations did not clearly answer this question either because result distributions by SED subcomponents were not tightly grouped. The lack of grouping, when the genetic algorithm had demonstrated a clear ability to achieve grouping, indicates that the most efficient method of achieving attenuation is not defined exclusively by control of velocity or control of spatial derivatives, but requires control of both. This conclusion is extrapolated to other forms of ASAC with the following statement. Efficient sensor selection and placement should consider multiple aspects of the structural response.

3.11 Conclusions

Various simulation tools were used to study the use of structural energy density in active structural acoustic control, resulting in the following conclusions and observations. First, in regard to control algorithms, the optimization space of SED is such that it can be minimized by straightforward means such as steepest descent or least-squares algorithms. Second, in regard to physical control hardware, it was observed that SED amplitude can be affected by mass loading in a lightweight structure, but the spatial distribution of SED is relatively unaffected. Optimal sensor and actuator location for SED-based ASAC is based on maintaining general symmetry relative to the disturbing force. Both sensor and actuator should avoid regions of high cross-derivative values. Third, in regard to performance, at optimally excited modal frequencies attenuation in SED at antinodes is proportional to the corresponding reduction in mean acoustic intensity. SED-based control is often superior to single-point velocity-based control and comparable in performance to two-point velocity-based control. A notable strength of SED-based control is the avoidance of unwanted amplification achieved through collocation of sensor and actuator in approximate symmetry to the disturbing force. SED may therefore be a good option for ASAC when a compact sensor is required. Fourth, in regard to ASAC in general, results of an efficiency-driven genetic optimization indicated that ASAC may benefit from sensor and actuator selection and placement such that each can operate by multiple mechanisms simultaneously. Finally, future work in SED-ASAC could extend to other types of structures and disturbances, and to the consideration of multiple sensors and actuators.

4 CONCLUSIONS

This chapter summarizes the key results of this thesis and makes recommendations for future work in registration and structural energy density-based active structural acoustic control.

4.1 Registration

The hybrid registration algorithm presented in this thesis demonstrated that the registration problem can be solved without the need for laser rangefinders or correct optimization initialization. This reduces the precision and amount of up-front work required to perform registration. This was accomplished in part by generating candidate solutions using a highly stable optimization method which converges almost regardless of the quality of initialization. Completion of the solution process was achieved through application of filtering criteria to eliminate inherently wrong solutions, and through the probabilistic consideration of a secondary error metric which allowed candidate solutions to be classified and the correct solution identified

A general linear laser model was also demonstrated in this thesis. It allows the primary model of the SLDV to be removed from the registration process and replaced with a universal slope-intercept form. This allows the hybrid registration algorithm to be used with any SLDV, independent of its unique optical behavior and length units system. The linear nature of the model also eliminates the use of iterative measures in laser model inversion as well as the need for numerical derivatives in optimization. Additionally, it eliminates the laser spherical

coordinate system from the registration process, leaving only the simpler laser and structural Cartesian coordinate systems. One final benefit of the general linear laser model demonstrated through the hybrid algorithm mathematics is that it allows for seamless transfer of data between all stages of the registration process, up to and including the application of results via intersection with the structure and velocity component identification.

This thesis also presented the use of an innovative method of experimentally validating a registration algorithm. This method overcomes the lack of information about true registration solutions by using a comparison of registration solutions calculated before and after a structure is moved in a deterministic manner. This method was applied to validate the hybrid registration method using a specially prepared plastic pipe and a large number of registration points. For a pipe z-axis rotation of 150 degrees, the comparison of hybrid algorithm results before and after rotation indicated a z-axis rotation of 149.7 degrees. This close agreement substantiates the effectiveness of hybrid registration.

In the spirit of the popular self-help book series, the hybrid algorithm presented here was developed as a kind of "registration for dummies". Once coded, it can be run as a black box. It has no settings to adjust and requires only a minimum of user input and comprehension. It does not, however, eliminate the need for accuracy when marking and targeting registration points.

Future work in developing registration could include the following.

- Exploration of direct-solve methods for the registration problem using the general linear laser model: The general linear laser model is very similar to the common pinhole camera model used in computer vision. It may be possible to adapt camera calibration techniques to perform laser registration.

- Exploration of the relationship between registration point arrangement and the number of distinct minima found in the standoff distance optimization space: If the number of expected distinct minima could be pre-determined, generation of candidate solutions could be discontinued when that number had been found, rather than using increased computation time to obtain a probabilistic assurance.
- Development of a weighting method for standoff distance optimization to decrease the effects of registration points with large marking and targeting error.

4.2 Structural Energy Density Based ASAC

A feasibility and performance study on the novel use of structural energy density in active structural acoustic control was presented in this thesis. Simulations of SED control on a flat plate were used to study issues of controllability and mass loading, sensor and actuator placement, and performance relative to single and dual-point velocity control.

The controllability of SED was shown to be nearly ideal by analysis of the contours of SED resulting from varying the gain between disturbance and control actuators. Mass loading was shown to affect SED amplitude while leaving its distribution relatively unaffected.

Proper sensor placement was determined to coincide with locations that are symmetric to the disturbing force, either by geometric symmetry, or by the similarity of antinodes. Proper actuator placement coincides with locations that are diagonally symmetric relative to the disturbing force. Both sensor and actuator placements should avoid regions of high cross derivative.

SED-based control was shown to achieve attenuations in mean acoustic intensity comparable to those achieved by single-point and sometimes dual-point velocity control. The collocation of sensor and actuator was demonstrated to temper the control results, slightly

decreasing attenuation of the fundamental mode, but severely limiting unwanted amplification when compared to single point velocity control.

Although SED-based ASAC was not shown to achieve any large improvements in areas such as attenuation and insensitivity to sensor placement, it may nonetheless be a good option when a compact sensor is required because of its resistance to unwanted amplifications. However, if the sensor is placed at a location where SED is not observable, amplification may still occur. Unfortunately, the observability of SED is only slightly better than that of velocity.

Future work in developing SED-based ASAC could include the following.

- Exploration of the use of multiple sensor and actuators. Performance may improve with multiple sensors as observability is increased and neither symmetry nor velocity is excluded when considering sensor placement.
- Exploration of application to other structure types and sizes. One structure which may be worthy of study is the thin-walled cylinder typical of aerospace applications of active control.
- Exploration of the use of PVDF films in creating large-area SED sensors. A larger sensor may improve observability.
- Characterization of SED-based ASAC when applied within an enclosure (likely to be a very computationally intensive undertaking).

REFERENCES

1. Wang, B., Burdisso, R.A., and Fuller, D.R. (1994). "Optimal Placement of Piezoelectric Actuators for Active Structural Acoustic Control." *Journal of Intelligent Material Systems and Structures*, 5, 67-77.

2. Tan, C.C., and Hird, C.I. (1997) "Active Control of the Sound Field of a Constrained Panel by an Electromagnetic Actuator—an Experimental Study." *Applied Acoustics*, 52(1), 31-51.

3. Cazzolato, B.S., and Hansen, C.H. (1998). "Active Control of Sound Transmission Using Structural Error Sensing." *Journal of the Acoustical Society of America*, 104(5), 2878-2889.

4. Ro, J., and Baz, A. (1999). "Control of Sound Radiation from a Plate into an Acoustic Cavity Using Active Constrained Layer Damping." *Smart Materials and Structures*, 8, 292-300.

5. Sors, T.C., and Elliott, S.J., (1999). "Modelling and Feedback Control of Sound Radiation from a Vibrating Panel." *Smart Materials and Structures*, 8, 301-314.

6. Tanaka, N., and Kobayashi, K. (2006). "Cluster Control of Acoustic Potential Energy in a Structural/Acoustic Cavity." *Journal of the Acoustical Society of America*, 119(5), 2758-2771.

7. Liu, Z.S., Lee, H.P., and Lu, C. (2006). "Passive and Active Interior Noise Control of Box Structures Using the Structural Intensity Method." *Applied Acoustics*, 67, 112-134.

8. Berry, A. (2001). "Advanced Sensing Strategies for the Active Control of Vibration and Structural Radiation." *Noise Control Engineering Journal*, 49(1), 54-65.

9. Parkins, J.W., Sommerfeldt, S.D., and Tichy, J. (2000). "Narrowband and Broadband Active Control in an Enclosure using the Acoustic Energy Density." *Journal of the Acoustical Society of America*, 108(1), 192-203.

10. Vass, J., Šmíd, R., Randall, R.B., Sovka, P., Cristalli, C., and Torcianti, B. (2008). "Avoidance of Speckle Noise in Laser Vibrometry by the Use of Kurtosis Ratio: Application to Mechanical Fault Diagnostics." *Mechanical Systems and Signal Processing*, 22, 647-671.

11. Blotter, J.D., West, R.L., and Sommerfeldt, S.D. (2002). "Spatially Continuous Power Flow Using a Scanning Laser Doppler Vibrometer." *Transactions of the ASME*, 124, 476-482.

12. Zeng, X., Wicks, A.L., and Mitchell, L.D. (1996). "Geometrical Method for the Determination of the Position and Orientation of a Scanning Laser Doppler Vibrometer." *Optics and Lasers in Engineering*, 25, 247-264.

13. Lindholm, B.E. (1996). "Three-Dimensional Position Registration of a Scanning Laser Doppler Vibrometer." *Proceedings of the 14th International Modal Analysis Conference*, 830-836.

14. Coe, D.H. (1998). "Improving the Three Dimensional, Structural Velocity Field Reconstruction Process with Computer Vision." Dissertation, Virginia Polytechnic Institute and State University. Accessed 9-30-2010 at http://scholar.lib.vt.edu/theses/available/etd-8998-163252/unrestricted/maindhc.pdf

15. Montgomery, D.E., and West, R.L. (1994). "Position registration of scanning lasers for experimental spatial dynamics modeling." *Advances in Design Automation*, 69(1), 337-342.

16. Martarelli, M., Revel, G.M., and Santolini, C. (2001). "Automated Modal Analysis by Scanning Laser Vibrometry: Problems and Uncertainties Associated with Scanning System Calibration." *Mechanical Systems and Signal Processing*, 15(3), 581-601.

17. Chen, K., Chen, G., Pan, H., and Li, S. (2008). "Secondary Actuation and Error Sensing for Active Acoustic Structure." *Journal of Sound and Vibration*, 309, 40-51.

18. Piaud, J.B., and Nicolas, J. (1986). "Relationship Between Vibrational and Acoustical Intensity for an Infinite Flat Plate." *Journal of the Acoustical Society of America*, 80(4), 1114-1121.

19. Sakano, A., and Tanaka, N. (2003). "Active Progressive Wave Control of a Simply Supported Plate." *JSME International Journal, Series C*, 46(3), 867-872.

20. Tanaka, N., Snyder, S.D., Kikushima, Y., and Kuroda, M. (1994). "Vortex Structural Power Flow in a Thin Plate and the Influence on the Acoustic Field." *Journal of the Acoustical Society of America*, 96(3), 1563-1574.

21. Lau, S.K., and Tang, S.K. (2003). "Impacts of Structural-Acoustic Coupling on the Performance of Energy-Density Based Active Sound Transmission Control." *Journal of Sound and Vibration,* 266, 147-170.

22. Manwill, D.A., Fisher, J.M., Sommerfeldt, S.D., Gee, K.L, and Blotter, J.D. (2010). "On the Use of Energy Based Metrics in Active Structural Acoustic Control." *Proceedings of Meetings on Acoustics*, 9(065006), 1-9

23. Timoshenko, S., and Young, D. (1955). *Vibration Problems in Engineering*, D. Van Norstrand Co., Inc. 442.

24. Bouthier, O.M., and Bernhard, R.J. (1992). “Models of Space-Averaged Energetics of Plates.” *AIAA Journal*, 30(3), 616-623

25. Fahy, F., and Gardonio, P. (2007). *Sound and Structural Vibration*, Academic Press, 141.

26. Fuller, C.R., Hansen, C.H., and Snyder, S.D. (1991). “Active Control of Sound Radiation from a Vibrating Rectangular Panel by Sound Sources and Vibration Inputs: an Experimental Comparison.” *Journal of Sound and Vibration*, 145(2), 195-215.

APPENDIX A. CODE

This appendix contains the following code:

- **pyramidsimulation.m:** code for performing the simulated registration validation presented in Section 2.11
- **hybrid_registration.m:** general code for executing the hybrid registration algorithm
- **platesolution.m**: code for calculating the structural and acoustic response of a plate subject to a point force disturbance

```
% pyramidsimulation

%
% this file performs registration on a simulated data set representing a
% rectangular pyramid shape

% initialize
clear all
clc

% operator input-------------------------------------
Dnear = 3;
Dfar = 9;
PSmarked = [0,0,0; 3,0,0; 0,2,0; 3,2,0; 1.5,1,0.5];
offsets =[
    0.0460   -0.0530         0
    0.1590    0.0950         0
    0.0900   -0.1460         0
    0.1760   -0.0950         0
    0.1400   -0.0790         0];
% typically, slopes are an input as well, but in this case, they will be
% calculated from the transformation to maintain compatibility
% -----------------------------------------------------

% add noise to structural coordinates
deviation = [0.033   -0.009   -0.022
    0.012    0.024   -0.020
    0.006   -0.001    0.013
    -0.008   -0.013   -0.005
    0.033   -0.007    0.019];
PSactual = PSmarked+deviation;

% calculate simulated transformation
q = [10,2,3,1];
q = q/norm(q);
q1 = q(1); q2 = q(2); q3 = q(3); q4 = q(4);
R = [q1^2-q2^2-q3^2+q4^2, 2*q1*q2+2*q3*q4, 2*q1*q3-2*q2*q4;
    2*q1*q2-2*q3*q4, -q1^2+q2^2-q3^2+q4^2, 2*q2*q3+2*q1*q4;
    2*q1*q3+2*q2*q4, 2*q2*q3-2*q1*q4, -q1^2-q2^2+q3^2+q4^2];
T = [0.2,-0.3,-8].';

% calculate laser coordinates, distances, and slopes
N = size(PSmarked,1);
for n = 1:N
    PL(n,:) = (R.'*(PSactual(n,:).') + T).';
    d(n) = PL(n,3);
    dS = PL(n,:)-offsets(n,:);
    slopes(n,:) = dS/d(n);
end

% swap dimensions
S = slopes.';
I = offsets.';
PS = PSmarked.';
batchsize = 20;
```

```
% solve using 4 points
[R1,T1] = hybrid_registration(S(:,1:4),I(:,1:4),PS(:,1:4),...
    Dnear,Dfar,batchsize);

% calculate starting guess for 5 points
for i = 1:N
    Scalc = R1.'*PS(:,i)+T1-I(:,i);
    dstart(i,1) = Scalc(3);
end

% solve using 5 points
[R2,T2] = hybrid_registration(S,I,PS,Dnear,Dfar,batchsize,dstart);
```

```
% [R,T] = hybrid_registration(S,I,PS,Dnear,Dfar,batchsize,dstart)
%
% This algorithm solves for the registration transformation using the
% general linear laser model hybrid registration algorithm.
% It requires N registration points, N being >=4.
%
% S and I are of dimension 3xN and are the general linear laser model
% slopes and intercepts which describe the registration points.
%
% PS is of dimension 3xN and contains the Cartesian coordinates of the
% registration points.  The point ordering in S,I, and PS must match!
%
% Dnear and Dfar are the standoff distance estimates that form a large box
% around the test structure.
%
% batchsize is how many candidate solutions to generate between pool
% evaluations
%
% dstart is an optional input of dimension Nx1.  It is used to give a
% starting point in standoff distance optimization when the solution being
% calculated is an extension of a previous solution by the addition of more
% points.  Batchsize defaults to 1 when this argument is given.
%
% R is a rotation matrix and T is a translation vector.  They obey the
% following relationships which are used in applying registration results
% PS = R(PL-T)
% PL = R'*PS + T
% C = R*S/norm(R*S)
% PS = h*C + R(I-T)
%
% PL is a location expressed in laser coordinates
% C is the direction of the laser beam expressed in structural coordinates
% h is a parametric scaling factor
%
% default settings can be modified on lines 39-42 in this file.

function [R,T] = hybrid_registration(S,I,PS,Dnear,Dfar,batchsize,varargin)

% default settings ----------------------------
rmsdeltadtolerance = 1e-12;
rmsdeltaqtolerance = 1e-12;
maxdistanceiterations = 40;
maxqiterations = 40;
% ---------------------------------------------

% set flags
poolcomplete = false;
cleansolutions = 0;
if(nargin==7)
    batchsize = 1;
end

% trap error
N = size(S,2);
if(N<4)
    error('registration requires at least 4 points');
```

```
end

while(~poolcomplete)
    for candsoln = 1:batchsize

        % generate starting guess
        for i = 1:N
            d(i,1) = -(Dnear+rand*(Dfar-Dnear));
        end
        if(nargin==7)
            d = varargin{1};
        end

        % optimize standoff distances
        clear J E;
        distanceconverged = false;
        distanceiterations = 1;
        while(~distanceconverged)

            % calculate current estimate of laser spot locations
            for i = 1:N
                PL(:,i) = d(i)*S(:,i)+I(:,i);
            end

            % pair points and calculate solution elements
            paircount = 0;
            for i = 1:N-1
                for j = i+1:N
                    % counter
                    paircount = paircount+1;

                    % actual distance
                    D(paircount) = sqrt(dot(PS(:,i)-PS(:,j),...
                        PS(:,i)-PS(:,j)));

                    % estimated distance
                    Dprime(paircount) = sqrt(dot(PL(:,i)-PL(:,j),...
                        PL(:,i)-PL(:,j)));

                    % error
                    E(paircount,1) = D(paircount)-Dprime(paircount);

                    % derivatives of error
                    dEijdi(paircount) = (-1/Dprime(paircount))...
                        *dot(PL(:,i)-PL(:,j),S(:,i));
                    dEijdj(paircount) = (1/Dprime(paircount))...
                        *dot(PL(:,i)-PL(:,j),S(:,j));
                    dEijdk(paircount) = 0;
                end
            end

            % assemble jacobian matrix
            J = zeros(paircount,N);
            paircount = 0;
            for i = 1:N-1
```

```
        for j = i+1:N
            paircount = paircount+1;
            J(paircount,i) = dEijdi(paircount);
            J(paircount,j) = dEijdj(paircount);
        end
    end

    % update standoff distance estimates
    deltad = inv(J.'*J)*J.'*E;
    d = d - deltad;

    % check for convergence
    rmsdeltad = sqrt(sum(deltad.^2));
    if(rmsdeltad<rmsdeltadtolerance)
        distanceconverged = true;
    end

    % check for over-iteration
    distanceiterations = distanceiterations+1;
    if(distanceiterations>maxdistanceiterations)
        distanceconverged = false;
        break;
    end
end

clear J E;

% is this a clean solution?
if(~and(distanceconverged,(max(d)<0)))
    if(nargin==7)
        error('final optimization failed');
    end
    continue;
end

% update counter
cleansolutions = cleansolutions+1;

% get laser spot location
for i = 1:N
    PL(:,i) = d(i)*S(:,i)+I(:,i);
end

% calculate point connection vectors
paircount = 0;
for i = 1:N-1
    for j = i+1:N
        paircount = paircount+1;
        deltaPS(:,paircount) = PS(:,j)-PS(:,i); % 10a
        deltaPL(:,paircount) = PL(:,j)-PL(:,i); % 10b
    end
end

% initialize flags and quaternion
quaternionconverged = false;
```

```
q = rand(4,1);
iterationcount = 0;

% solve for rotation
while(~quaternionconverged)
    iterationcount = iterationcount+1;
    q = q/norm(q);
    q1 = q(1); q2 = q(2); q3 = q(3); q4 = q(4);

    % calculate rotation matrix
    R = [q1^2-q2^2-q3^2+q4^2, 2*q1*q2+2*q3*q4, 2*q1*q3-2*q2*q4;
        2*q1*q2-2*q3*q4, -q1^2+q2^2-q3^2+q4^2, 2*q2*q3+2*q1*q4;
        2*q1*q3+2*q2*q4, 2*q2*q3-2*q1*q4, -q1^2-q2^2+q3^2+q4^2];

    % calculate derivative matrices
    dRdq1 = [2*q1, 2*q2, 2*q3;
        2*q2, -2*q1, 2*q4;
        2*q3, -2*q4, -2*q1];
    dRdq2 = 2*[-q2, q1, -q4;
        q1, q2, q3;
        q4, q3, -q2];
    dRdq3 = 2*[-q3, q4, q1;
        -q4, -q3, q2;
        q1, q2, q3];
    dRdq4 = 2*[q4, q3, -q2;
        -q3, q4, q1;
        q2, -q1, q4];

    % calculate matrix system
    paircount = 0;
    for i = 1:N-1
        for j = i+1:N
            paircount = paircount+1;
            E(paircount*3-2:paircount*3,1) =...
                R*deltaPL(:,paircount)-deltaPS(:,paircount);
            dEijdq1 = dRdq1*deltaPL(:,paircount);
            dEijdq2 = dRdq2*deltaPL(:,paircount);
            dEijdq3 = dRdq3*deltaPL(:,paircount);
            dEijdq4 = dRdq4*deltaPL(:,paircount);
            J(paircount*3-2:paircount*3,1) = dEijdq1;
            J(paircount*3-2:paircount*3,2) = dEijdq2;
            J(paircount*3-2:paircount*3,3) = dEijdq3;
            J(paircount*3-2:paircount*3,4) = dEijdq4;
        end
    end

    % update estimate of quaternion
    deltaq = inv(J.'*J)*J.'*E;
    q = q - deltaq;
    q = q/norm(q);

    % check for convergence
    if(sqrt(mean(deltaq.^2))<rmsdeltaqtolerance)
        quaterionconverged = true;
    end
```

```
            % check for overiteration
            if(iterationcount>=maxqiterations)
                break;
            end
        end

        % calculate rotation matrix
        q1 = q(1); q2 = q(2); q3 = q(3); q4 = q(4);
        R = [q1^2-q2^2-q3^2+q4^2, 2*q1*q2+2*q3*q4, 2*q1*q3-2*q2*q4;
            2*q1*q2-2*q3*q4, -q1^2+q2^2-q3^2+q4^2, 2*q2*q3+2*q1*q4;
            2*q1*q3+2*q2*q4, 2*q2*q3-2*q1*q4, -q1^2-q2^2+q3^2+q4^2];

        % calculate translation vector
        for i = 1:N
            Tprime(:,i) = PL(:,i)-R.'*PS(:,i);
        end
        T = mean(Tprime,2);

        % calculate secondary error descriptor
        for i = 1:N
            uvw(:,i) = R.'*PS(:,i)+T-I(:,i);
            Sprime(:,i) = uvw(:,i)/uvw(3,i);
        end
        deltaS = S-Sprime;
        e2 = 0;
        for i = 1:N
            e2 = e2+deltaS(:,i).'*deltaS(:,i); % 13c
        end

        % store candidate solution
        E2(cleansolutions) = e2;
        bigR{cleansolutions} = R;
        bigT{cleansolutions} = T;
        bigD{cleansolutions} = d;

    end

    % check for completeness
    if(nargin==7)
        poolcomplete = true;
    else
        figure(1); clf;
        plot(sort(E2));
        disp('Is solution pool complete?');
        if(input('Input 1 if yes, 0 if no '))
            poolcomplete = true;
        end
    end
end

% select solution
[minerr,solutionindex] = min(E2);
R = bigR{solutionindex};
T = bigT{solutionindex};
```

```
% PLATESOLUTION vibration and radiation solver for simply supported plate
%     RESPONSE = PLATESOLUTION(INPUTS) uses a modal solution and a
%     discretized form of Rayleigh's integral to solve for the response.
%     INPUTS is a struct containing the following fields
%       .rho: volume density of plate material (kg/m^3)
%       .h: plate thickness (m)
%       .D: bending stiffness of the plate (N-m)
%       .eta: structural damping coefficient
%       .Lx: size of plate in x-dimension (m)
%       .Ly: size of plate in y-dimension (m)
%       .M: number of modes ot use in x-direction
%       .N: number of modes to use in y-direction
%       .xf: x location of forcing
%       .yf: y location of forcing
%       .F: complex force amplitude
%       .w: angular frequency of forcing
%       .vxpts: number of points to measure velocity at on structure in x
%       .vypts: number of points to measure velocity at on structure in y
%       .pxpts: number of points to measure pressure at in x
%       .pypts: number of points to measure pressure at in y
%       .pxstart: lower x limit of pressure planes
%       .pxstop: upper x limit of pressure planes
%       .pystart: lower y limit of pressure planes
%       .pystop: upper y limit of pressure planes
%       .z1: height of first pressure plane
%       .z2: height of second pressure plane
%       .z3: height of third pressure plane
%     RESPONSE is a struct which contains a copy of INPUTS as well as the
%     following fields:
%       .W: plate complex displacement amplitude
%       .W___: spatial or temporal derivative of complex displacement
%       amplitude, the type of derivative being indicated by the letters
%       that replace the underscores shown here
%       .P1: complex pressure on first plane
%       .P2: complex pressure on second plane
%       .P3: complex pressure on third plane
%       .vxvec: x-vector of structural response sampling
%       .vyvec: y-vector of structural response sampling
%       .pxvec: x-vector of acoustic response sampling
%       .pyvec: y-vector of acoustic response sampling

function reponse = platesolution(inputs)

% transfer data
reponse = inputs;

% unpack inputs
rho = inputs.rho;
h = inputs.h;
D = abs(inputs.D);
eta = inputs.eta;
a = inputs.Lx;
b = inputs.Ly;
N = inputs.N;
M = inputs.M;
xf = inputs.xf;
```

```
yf = inputs.yf;
F = inputs.F;
w = inputs.w;
vxpts = inputs.vxpts;
vypts = inputs.vypts;
pxpts = inputs.pxpts;
pypts = inputs.pypts;
pxstart = inputs.pxstart;
pxstop=inputs.pxstop;
pystart = inputs.pystart;
pystop = inputs.pystop;
z1 = inputs.z1;
z2 = inputs.z2;
z3 = inputs.z3;

% prepare storage
reponse.W = zeros(vxpts,vypts);
reponse.Wx = zeros(vxpts,vypts);
reponse.Wy = zeros(vxpts,vypts);
reponse.Wxxx = zeros(vxpts,vypts);
reponse.Wxx = zeros(vxpts,vypts);
reponse.Wxy = zeros(vxpts,vypts);
reponse.Wxxy = zeros(vxpts,vypts);
reponse.Wxt = zeros(vxpts,vypts);
reponse.Wyt = zeros(vxpts,vypts);
reponse.Wyy = zeros(vxpts,vypts);
reponse.Wyyx = zeros(vxpts,vypts);
reponse.Wyyy = zeros(vxpts,vypts);
reponse.Wt = zeros(vxpts,vypts);
reponse.P1 = zeros(pxpts,pypts);
reponse.P2 = zeros(pxpts,pypts);
reponse.P3 = zeros(pxpts,pypts);
reponse.vxvec = linspace(0,a,vxpts);
reponse.vyvec = linspace(0,b,vypts);
reponse.pxvec = linspace(pxstart,pxstop,pxpts);
reponse.pyvec = linspace(pystart,pystop,pypts);

% solve for structural response
for m = 1:M
    for n = 1:N

        % calculate wmn
        wmn = sqrt(D/(rho*h))*((m*pi/a)^2+(n*pi/b)^2);

        % create scaling terms
        mpa = m*pi/a;
        npb = n*pi/b;
        force_term = sin(mpa*xf)*sin(npb*yf);
        damping_term = (wmn^2-w^2-1i*eta*wmn^2)/...
            ((wmn^2-w^2)^2+(eta*wmn^2)^2);
        Q = force_term*damping_term;

        % calculate modal contributors
        sx = sin(m*pi*reponse.vxvec/a);
        sy = sin(n*pi*reponse.vyvec/b);
        cx = cos(m*pi*reponse.vxvec/a);
```

```
        cy = cos(n*pi*reponse.vyvec/b);
        cs = cx'*sy;
        sc = sx'*cy;
        ss = sx'*sy;
        cc = cx'*cy;

        % calculate response
        reponse.W = reponse.W+Q*ss;
        reponse.Wxy = reponse.Wxy+mpa*npb*Q*cc;
        reponse.Wxx = reponse.Wxx-Q*mpa*mpa*ss;
        reponse.Wyy = reponse.Wyy-npb*npb*Q*ss;
        reponse.Wxxy = reponse.Wxxy-mpa*mpa*npb*Q*sc;
        reponse.Wyyx = reponse.Wyyx-mpa*npb*npb*Q*cs;
        reponse.Wxxx = reponse.Wxxx-mpa*mpa*mpa*Q*cs;
        reponse.Wyyy = reponse.Wyyy-npb*npb*npb*Q*sc;
        reponse.Wxt = reponse.Wxt+mpa*Q*cs;
        reponse.Wyt = reponse.Wyt+npb*Q*sc;
    end
end

% correct scaling
st0 = 4*F/(a*b*rho*h);
reponse.Wx = reponse.Wxt*st0;
reponse.Wy = reponse.Wyt*st0;
reponse.Wxt = 1i*w*st0*reponse.Wxt;
reponse.Wyt = 1i*w*st0*reponse.Wyt;
reponse.Wt = st0*1i*w*reponse.W;
reponse.Wtt = reponse.Wt*1i*w;
reponse.W = st0*reponse.W;
reponse.Wxx = st0*reponse.Wxx;
reponse.Wyy = st0*reponse.Wyy;
reponse.Wxy = st0*reponse.Wxy;
reponse.Wxxx = st0*reponse.Wxxx;
reponse.Wxxy = st0*reponse.Wxxy;
reponse.Wyyx = st0*reponse.Wyyx;
reponse.Wyyy = st0*reponse.Wyyy;

% calculate constants and locations and initialize storage
freq = w/(2*pi);
lambda = 343/freq;
k = w/343;
scale = 1i*1.21*343/lambda;
PX = zeros(length(reponse.pxvec),length(reponse.pyvec));
PY = zeros(length(reponse.pxvec),length(reponse.pyvec));
for px = 1:length(reponse.pxvec)
    for py = 1:length(reponse.pyvec)
        PX(px,py) = reponse.pxvec(px);
        PY(px,py) = reponse.pyvec(py);
    end
end
delZ1 = z1*ones(size(PX));
delZ2 = z2*ones(size(PX));
delZ3 = z3*ones(size(PX));
Psize = ones(size(PX));
ds = (reponse.vxvec(2)-reponse.vxvec(1))*(reponse.vyvec(2)-reponse.vyvec(1));
```

```
% calculate pressure response
for vx = 1:length(reponse.vxvec)
    for vy = 1:length(reponse.vyvec)
        x = reponse.vxvec(vx);
        y = reponse.vyvec(vy);
        u = reponse.Wt(vx,vy)*Psize;
        delx = x*Psize-PX;
        dely = y*Psize-PY;
        r1 = sqrt(delx.^2+dely.^2+delZ1.^2);
        r2 = sqrt(delx.^2+dely.^2+delZ2.^2);
        r3 = sqrt(delx.^2+dely.^2+delZ3.^2);
        reponse.P1 = reponse.P1+(u./r1).*exp(-1i*k*r1);
        reponse.P2 = reponse.P2+(u./r2).*exp(-1i*k*r2);
        reponse.P3 = reponse.P3+(u./r3).*exp(-1i*k*r3);
    end
end

% correct scaling
reponse.P1 = ds*scale*reponse.P1;
reponse.P2 = ds*scale*reponse.P2;
reponse.P3 = ds*scale*reponse.P3;
```